UNIVERSITÁ DEGLI STUDI DI PADOVA

FACOLTÀ DI SCIENZE MM. FF. NN

Dipartimento di Geoscienze

Direttrice Prof. Cristina Stefani

Corso di Laurea magistrale in Geologia e Geologia Tecnica

TESI DI LAUREA MAGISTRALE IN GEOLOGIA E GEOLOGIA TECNICA

Effect of a weak layer at the lithosphere-asthenosphere boundary on subduction dynamics

Relatore: Dott.Manuele Faccenda

Co-relatore: Prof. Dott.Boris Kaus

Laureanda: Carluccio Roberta

Anno accademico 2015/2016

11 Marzo 2016

Abstract

The aim of this thesis is to investigate and identify the first order effects of a weak layer at the lithosphere asthenosphere boundary (LAB) on a subduction zone, as to date, no previous geodynamics studies on this topic exist. The models developed are focussed on the study of a dynamically induced subduction through the use of 2-D and 3-D mechanical models involving a visco-plastic rheology. The results revealed that the process of an oceanic lithosphere subducting into the mantle can exhibit a wide range of behaviours depending on the weak layer characteristics such as its viscosity and density. Morphological and kinematic investigations of the time evolution of the model have allowed a correlation between the subduction plate velocity and the viscosity and density contrast between mantle and weak layer to be defined. Four possible subduction regimes were established, constraining the role of a weak layer for the parameters modelled. Therefore, the possible existence of a weak layer at the lithosphere asthenosphere boundary on subdution dynamics can affect subduction. From this study emerged an overall advancing trend for the plate with the resultant motion dependent on the constrained characteristics of the weak layer.

Contents

1 Introduction

Subduction zone dynamics are a key process in plate tectonics and so it is important to have a better understanding through geodynamics modelling. The base of the lithosphere, the lithosphere–asthenosphere boundary (LAB), is fundamental to the understanding of how plate tectonics work. However an exact understanding of the mechanisms, for example, those that give rigidity to the plates and defines their thickness remain elusive and highly debated. Plate tectonics have been fundamental to the Earth sciences for almost 50 years. Important questions still remain though, such as: 'Where is the base of a plate?', 'What makes a plate 'plate-like'?', and 'How does the mantle drive plate tectonics?'. In this scenario, the possible existence of a localised channel at the lithosphere asthenosphere boundary could have implications for the driving forces of plate tectonics and mantle dynamics.

The aim of this thesis is to investigate and identify the first order effects of a weak layer at the lithosphere asthenosphere boundary on a subduction zone.

Modelling the effects of a weak layer at the LAB on a subduction zone is challenging because there are no previous geodynamics study on this topic and because currently the origin and nature of these channels is not well understood, also there is not a good constraint on where they exist. Despite seismic images detecting the presence of a low velocity layer at base of an oceanic subducting lithosphere, its effects and role on subduction dynamics still remain elusive. Further details are available in section 1. This thesis will focus on the study of dynamically induced subduction involving the presence of a weak layer at the base of an oceanic subducting lithosphere through the use of 2-D and 3D mechanical models involving a visco-plastic rheology. Further details are available in section 2. The investigation of the first order effects of a weak layer at the LAB on subduction dynamics aims to constrain the influence of several important parameters, such as viscosity, density and thickness using 2D and 3D geodynamics modelling. Further details are available in section 3. By modelling these processes, the first order effects such as the possible generation of a variety of subduction regimes were constrained as a function of the parameters modelled. Further details are available in section 4. Finally, the possible existence of a weak layer at the base of an oceanic plate can affect subduction, either promoting or impeding convection in the mantle depending on its nature. However,

other factors not considered here for simplicity, could also play a role in defining the controls of the weak layer (WL) on the subduction dynamics. This thesis intentionally applies to a simple model in order to understand first-order physical principles and effects as no previous study on this topic exist.

Future investigations will concentrate on exploring the role of other factors, such as those involving temperature dependent visco-elasto-plastic rheology and also on the phenomena induced by the presence of an overriding plate in order to gain a more in-depth understanding.

1.1 Literature review

The basics principles and concepts of plate tectonics and lithosphere-asthenosphere boundary are presented here in order to gain an understanding and to study the effect of a weak layer at the LAB on subduction dynamics. It's important to consider the basic principals before investigating the complexity of the problem posed by this thesis because there are no other previous geodynamic studies on this topic.

First, by the introduction of the concepts of plate tectonics and mantle convection, secondly by the description of the surface motion kinematics with the development of the toroidal and poloidal flow, followed by the definition of the plate forces acting on subduction zones and related geodynamics settings. Finally, focussing on summarising what is known from the literature about the nature of the lithosphere-asthenosphere boundary and the potential presence of a weak layer at the base of a tectonic plate.

1.1.1 Plate tectonics

Plate tectonics is a unifying working hypothesis which provides a kinematic model of the upper layer of the Earth (Le Pichon et al. (2013)). The idea of plate tectonics was born at the beginning of the XXth century, when closer examinations of the globe resulted in the observation that most of the continents seemed to fit together like a puzzle. In 1912 Alfred Wegener (1880-1930) developed the concept that continents were once squeezed into a single protocontinent called Pangea, and over the time they have drifted apart to their current distribution. Wegener's theory of continental drift, lacked a solid geological mechanism to explain how the continents could drift across the Earth's surface as he proposed. In the 1930s, Arthur Holmes

hypothesised that thermal convection in the Earth's mantle provides the necessary driving force for plates motion.

Nonetheless, plate tectonics still remains to this day one of the most successful theories in physics. It can be used to make quantitative predictions on most of the phenomena studied by the different disciplines of the Earth's sciences (e.g. the distribution and magnitude of seismic and volcanic disasters (see Abbott (2008)) and is likely a key factor for planetary habitability.

Plate tectonics is purely a kinematic model that describes the plate motion whereas the theory of mantle convection describes and incorporates the essential dynamics and the energy sources for plate motion. Mantle convection is widely believed to be the direct energy source of solid Earth dynamics and all its features, and is believed to be generated from a combination of radioactive decay, cooling, adiabatic and shear heating.

Several forces act on plates which can either increase or impede their relative motion. Buoyancy is one of these multiple forces. The slab pull forces which is the negative component of the buoyancy force, is the most most important of the plate forces (Forsyth and Uyeda, 1975) and develops in subduction zone.

From a dynamic point of view the lithospheric plates are an integral part of the mantle convection (i.e. of the upper layer). However, there is still no complete physical theory which predicts how plate tectonics is entirety driven, or caused by mantle convection, Bercovici et al. (2000).

Thus, a unifying theory of mantle dynamics and plate tectonics (i.e. a theory of mantle convection that generates plates) is still one of the biggest challenges of geodynamics and geophysics (Bercovici (2003); Ricard (2007); Turcotte and Schubert (2014)).

1.1.1.1 Plate kinematics

Plate surface motion is well defined by solid-body rotations of spherical caps. The mathematical working model of plate tectonics has the Euler pole theory as a core premise and continues to be used in present-day plate motion models. The motion of the plates at the surface gives an accurate prediction of the deformation at the plate boundaries. The relative motion at the boundary can be either divergent, convergent or shear.

Solid-body motion with narrow boundaries can describe the plate kinematics. However the Euler poles (e.g. directions of motion) appear largely uncorrelated. These features lead to a system of plate boundaries where

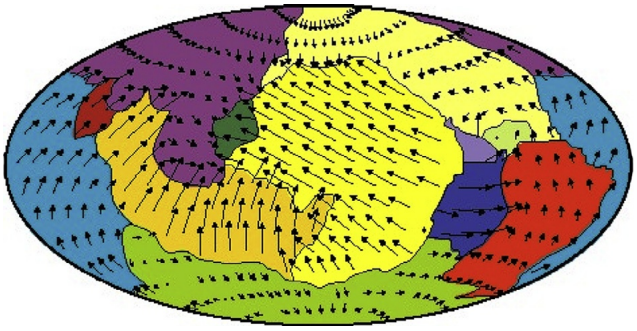

Fig. 1: Configuration of present-day plate tectonics with indicated directions of motion, on equal area-projection map. Surface motion is divided into 12 major caps or plates. Plates edges define their boundaries and a series of minor plates and micro-plates (from Bercovici (2003)).

there is nearly as much strike-slip shear deformation as there is divergent and convergent motion, which is an important enigma about the plate-tectonic style of mantle convection, see fig. 1. For more details see Bercovici (2003).

Closely related to these modes of plate boundary deformation is the composition of the present-day velocity field in terms of poloidal, $\vec{v}_p$, and toroidal components, $\vec{v}_t$. Poloidal flow is essentially the vertical convective circulation that essentially corresponds to the rise and fall of plates in the vertical plane ($\vec{\Delta} \times \vec{\Delta_p} = \vec{0}$), and is associated with vertical mass transport. It expresses itself as convergent and divergent motion at the surface. Toroidal flow corresponds to vortex-like flow and rigid body rotation ($\vec{\Delta} \cdot \vec{v}_t = 0$). Thus, it involves horizontal spinning or shearing motion about a vertical axis (e.g., cyclonic activity in the atmosphere). In plate motions, this is manifested primarily as a strike-slip shear. The fig. 2 shows the poloidal and toroidal components of the velocity field in the three dimensions. For further details see section 4.2.

1.1.1.2 Plate forces The mathematical or Euler pole theory of plate tectonics is a kinematic representation of motion, but not causative since it doesn't describe the dynamics or the driving forces for plate tectonics, see Bercovici (2003). Whether the forces between plate and mantle impede or advance motion, depends on the relative motion between the plates and mantle. A combination of plate forces is responsible of surface plates movement.

A simplified overview of the forces that can affect the movement of lithospheric plates is provided in fig. 3. The relative contribution of these forces

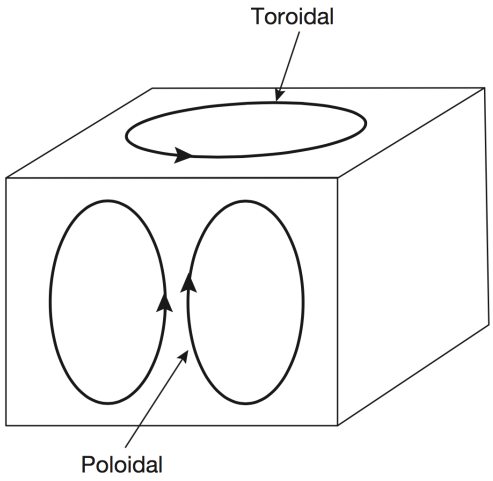

Fig. 2: Diagram illustrating simple flow lines associated with toroidal and poloidal motion (from Bercovici (2003)).

to plate motion can be explored dividing the plate forces into two categories:

1. forces acting at the lithosphere base;

2. forces acting at plate margins.

Forces acting at the base of lithospheric plates Lithospheric plates are decoupled from the rest of the mantle because the underlying asthenosphere is weaker, however, plates may be driven by forces imparted by the convecting mantle. F_{DO} can be consider the ocean driving force acting underneath the oceanic plate when a lithosphere is carried out by a faster moving asthenosphere. Conversely, if the asthenosphere is moving slower or in the opposite direction of plate, then the force acting at the base of the oceanic plate can be considered as an ocean drag force, R_{DO}, and thus impedes the movement of the plate.
The continental lithosphere can also be associated with an additional continental drag force, R_{DO}. This is due to the fact that continents almost always have a "keel", and so may develop a higher resistance to movement than for oceanic plates. The resulting resistive force acting on the base of a continental plate would be the sum of both oceanic and continental drag forces $R_{\mathrm{DO}} + R_{\mathrm{DC}}$, (Rogers and Blake (2008)).

Forces acting at plate margins Other forces acting on plates are generated at their boundaries. At constructive boundaries, an oceanic plate

can experience a sub-horizontal force which acts away from the ridge, the ridge-push force (F_{RP}). At mid ocean ridges, the up welling of hot mantle material can generates a positive buoyancy effect. The ridge resistance, (R_{R}) is the encountered resistance to movement at these localities. An additional retarding force is R_{TF}, the transform fault resistance force.

At destructive plate boundaries the major component is the negative buoyancy force which is a gravity-generated force that pulls the whole oceanic plate down as a result of the negative buoyancy of the slab. The component of this down-ward-acting force that is transmitted to the plate is the slab-pull force, (F_{SP}). The slab pull force acts downward bending the slab both promoting and driving the collapse of an oceanic lithosphere into the mantle material. It's magnitude is related to the angle at which the slab descend into the mantle. However, the sinking slab encounters resistance as it descends called the slab resistance force, R_{S}. This resistive force is a combination of the frictional drag acting on its upper and lower surface and from the viscosity of mantle material that is being displaced.

Furthermore, the downwards moving plate must flex at the trench before fore it begins to slide beneath the opposing plate. This provides a further resistance to the plate motion called bending resistance, R_{S} as downwards moving plates must flex at the trench before sliding beneath opposite plates.

Other forces can be due to i) the pushing of the subducting slab against the overriding plate: the overriding plate resistance, R_{O}; ii) the possible associate trench suction force F_{SU} (analogous to the ocean driving forces for overriding plate); iii) trench suction force F_{SU} derived from a convection induced in the mantle above the subducting lithosphere and serves to pull the plate toward the trench; iiii) a collisional resistance force R_{CR} generated by the collision of plates. This acts in the opposite direction within each converging plate, but is equal in magnitude to both (Rogers and Blake (2008)).

The velocity of present day motion appear to be constant, indicating a state of dynamic equilibrium where a balance exist between the driving and resistive forces. However, each plate moves at its own rate, which suggest that the relative importance of the driving and retarding forces must vary from plate to plate. The driving agent of plate tectonics is also a composite of these several forces. The classic demonstration of this force system was done in the seminal paper of Forsyth and Uyeda. Some of these forces can

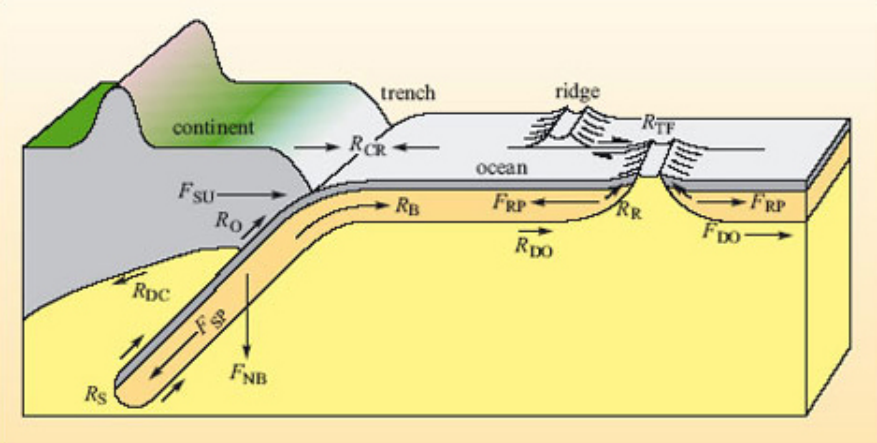

Fig. 3: Figure illustrating the forces acting on tectonic plates (fromRogers and Blake (2008)).

be shown to be more important than others, and some are insignificant. It's believed that slab pull is the most important of the plate forces (i.e., one order of magnitude stronger than the other forces) and subducting slabs are basically cold downwellings, Forsyth and Uyeda (1975). Since, observations has revealed that plates velocity strongly correlates with the connectivity of a plate to a slab (i.e., the percent of its perimeter taken by subduction zones) and so its trench length, while it does not correlate with its ridge length (Forsyth and Uyeda, 1975). Thus, it's generally accepted that plates are not so much driven by convection but are infarct an integral part of mantle circulation, and so mantle convection (Bercovici (2003); Ricard (2007); Turcotte and Schubert (2014)). Other feature such as, plate size have little correlation with plate velocity, which is either due to the lack of mantle drag or that mantle drag and distributed ridge push balance each other (Hager and O'Connell, 1981).

1.1.1.3 Subduction zone A subduction zone is a convergent plate boundary where an oceanic plate subducts beneath an other plate, due to higher density. Both slab pull and ridge push forces develops in the oceanic lithosphere and are both caused by variation of the potential energy along the oceanic lithosphere.

As the most important of the plate forces is slab pull and develops in subduction zone. Then the subduction of an oceanic lithosphere into the Earth's mantle is one of the key processes of plate tectonics and one of the most studied phenomena.

The oceanic lithosphere is continuously created at mid ocean ridges. At these constructive margins the new hot material floats on the underlying mantle. As it moves far away from the ridge it becomes continuously denser and denser over time, due to cooling and thickening. When the oceanic lithosphere is heavier than the surrounding mantle a gravitational instability is generated and the oceanic lithosphere sinks into the mantle. The heavier and colder oceanic material continues to subduct into the mantle as long as it is denser than the surrounding rocks, Turcotte and Schubert (2014).

1.1.2 The lithosphere-asthenosphere boundary (LAB)

The lithosphere-asthenosphere boundary, or LAB, is the boundary between the Earth's lithosphere and asthenosphere. The lithosphere is a mechanical concept which implies strength and relative permanence, whereas asthenosphere was originally defined as "the weak layer" of the upper mantle, Anderson (1995). In geodynamics, at the LAB is generally associated an isotherm of 1300 °C, and the lithosphere and mantle are described as a conductive and convective layers respectively (Artemieva and Mooney (2002)).

Since, the plate tectonic model relies on the concept of a relatively rigid lid moving over a weaker asthenosphere, the lithosphere-asthenosphere boundary (LAB) is a first order structural discontinuity that accommodates differential motions between tectonic plates and the underlying mantle. It is also the most extensive of plate boundary on the planet (Kawakatsu et al. (2009)). Thus, the LAB is fundamental to our understanding of how plate tectonics works. However the nature, depth and defining mechanisms of the boundary are still not completely understood and the LAB is a hot debated topic in the academic world.

From the works of Fischer et al.; Schmerr; Sakamaki et al.; Rychert et al.; Rychert et al.; Rychert and Shearer has been recognised the presence of:

1. a low-velocity zone observed at depths of 50 to 220 km associated with a transition from a fast seismic lid to a slower deeper layer.
2. a possible interface which correlates with the tectonic environment: shear velocity drops at an average depth varying from 95 ± 4 kilometres beneath Precambrian shields and platforms to 81±2 kilometres beneath tectonically altered regions and ca.70±4 kilometres at oceanic island stations, revealed by 15 years of global seismic data;
3. a evidence for a sharp seismic discontinuity, which represents a velocity reduction of 5 to 10 per cent across a sharp boundary no more than

20 km thick, obtained by regional studies;

4. This discontinuity likely represents the LAB under oceans and tectonically altered regions, but it may constitute another boundary in cratonic regions where the lithosphere-asthenosphere horizon is thought to be much deeper.

These conclusions have been obtained constraining the depth of the LAB and its associated isotropic, and/or anisotropic velocity gradients, from a wide range of seismic investigations and analysis methods. Surface-wave tomography can provide robust constraints on three-dimensional, whereas absolute shear-wave velocity structure at lithospheric and asthenospheric depths, at both regional and global scales. In addition, vertical variations in velocity anisotropy from surface-wave tomography have also been used to define the LAB, including changes in the strength and orientation of both radial and azimuthal anisotropy.

1.1.2.1 The nature of the lithosphere-asthenosphere boundary The origin of the seismic discontinuity associated with the LAB, it's also known as the Gutenberg discontinuity (G), still remains enigmatic. At this boundary the wave velocity decreases because rocks may experience a variation in some of their physical and rheological properties, for example density, bulk modulus, shear modulus, viscosity, temperature and water availability. Infact, rheological investigations of the LAB using glacial rebound and gravitational constraints reveal a one to two order of magnitude decrease in mantle viscosity across the interface, Mitrovica and Forte (1997).

Numerous hypotheses have been proposed to explain the origin of the low velocity zone (LVZ) and associated lowered viscosities ranging from: temperature, hydration, compositional variations, grain size, and anisotropy to the presence of melt $\pm$ the presence of volatile, see also Schmerr (2012). If temperature was the only mechanism responsible for the origin of the LAB, then it would be expected a gradual transition between the two layers. Instead high resolution images have revealed that the transition is sharp. Also, a purely anisotropic interpretation for the observed seismic velocity discontinuity wouldn't necessary represent the LAB because anisotropicity could be frozen into the plate from a previous episode of deformation.

This lead to the hypothesis that water or melt present in this channel could weaken the mantle and define the base of the plate. An increase in hydratation with depth could be related to the shallow dehydratation

that occurs during plate formation at mid-ocean ridge. Whereas melt could be caused by complex mantle flow from subduction tectonics and/or melt ponding, probably also promotes by the presence and storage of volatile within this discontinuity, for more details see Sakamaki et al. (2013). Further investigations are needed to find the origin of any existing melt, because normal oceanic lithosphere is predicted to be cold at a depth of 73 km and so is not necessarily predicted to melt, for more details see Rychert (2015) .

1.1.3 Seismic image of the slippery base of a tectonic plate

Reflection seismic image analysis of the base of the Pacific tectonic plate subducting underneath the Australian plate reports a v_p drop of 10±4 %, corresponding to a "low-seismic-wave-channel" of 8-12 km thick at a depth of 100 km which corresponds to the LAB Stern et al. (2015), see fig. 4. For Stern et al. the presence of the low viscosity channel with distinct attributes, such as high strain/strain rate and high shear stresses can be due to partial melt ± volatile and/or hydrated phases. Stern et al., also suggests that the thin channel decouples the lithosphere from the asthenosphere, allowing plate tectonics to occur. Plate tectonics has been fundamental to the Earth sciences for almost 50 years. However, important questions remain, such as, where is the base of a plate and what makes a plate 'plate-like'? How does the mantle drive plate tectonics? In fact the existence of the channel itself is still enigmatic. How and why channelization would occur over a 10-km depth range is also not known.

Overall, channels offer a plausible explanation for some of the elusive nature of the LAB. Narrow channels would be nearly imperceptible in seismic imaging methods that rely on low-frequency waves, which might explain why LAB detection is intermittent and discrepant between methods. For a full understanding of such channels, better constraints on where they exist is needed. Finally, the implications of these channels for the coupling of the plates to the underlying asthenosphere and the driving forces of plate tectonics can be answered by incorporating tight seismic constraints with laboratory experiments and geodynamical modelling(Rychert, 2015; Stern et al., 2015).

1.2 Motivations and aim

The aim of this thesis is to explore the first order effects of a weak layer at the lithosphere-asthenosphere boundary on subduction dynamics through the constrained analysis of the influence of several important parameters, such as viscosity, density and thickness using 2D and 3D geodynamics modelling. Through a deep investigation of these parameters, the question to be addressed is: "does a weak layer at the base of an oceanic plate play any role on subduction dynamics?".
The two main motivations for this study are:

1. no previous geodynamic numerical studies on this topic despite seismic images detecting the presence of a low velocity layer at base of an oceanic subducting lithosphere;
2. the subduction zone related dynamics are a key process in plate tectonics and is important to have a better understanding through geodynamics modelling;

The idea of this master thesis arises from a paper recently published in 'Nature': "A seismic reflection image for the base of an oceanic plate" by Stern et al. (2015). In Fig. 4, is shown a high-resolution seismic reflection image of the base of the Pacific oceanic plate as it descends beneath New Zealand, revealing a 10 kilometer thick channel that decouples the plate from the underlying upper mantle. More details can be found in section 1.1.3.

However, reproducing the Australian-New Zealand subduction zone is outside the scope of this thesis because:

1. no previous geodynamics models on this topic exist and so in order to understand first-order physical principles and effects, this Master thesis intentionally applies to a simple model;
2. the numerical computational codes used in this project are under development and this complicated the process of obtaining a numerical results for the problem within the limited time of the project.

The following analysis procedure was developed in order to address the main question of this thesis consisting in 2 steps:

1. Perform validation simulations using 2D, simple geometrical and rheological models, using the MVEP2 code (see appendix A);

2. Study the effects of a weak layer at the LAB boundary on subduction dynamics for 2D and 3D models using the LaMEM code.

Initially validation models were developed for a linear rheology case using MVEP2, and can be seen in appendix A. Secondly, comparable 2D results were obtained using LaMEM. During the development of the 3D models, a numerical instability was encountered and is shown in appendix A. In order to overcome this instability, the previous model setup was adapted for solving the problem of this thesis as it shown in fig. 8. Once the base model simulations were working correctly, results were then obtained to study the effect of a WL on the subduction dynamics by changing either the vertical viscosity or density structure of the models as well as the thickness.

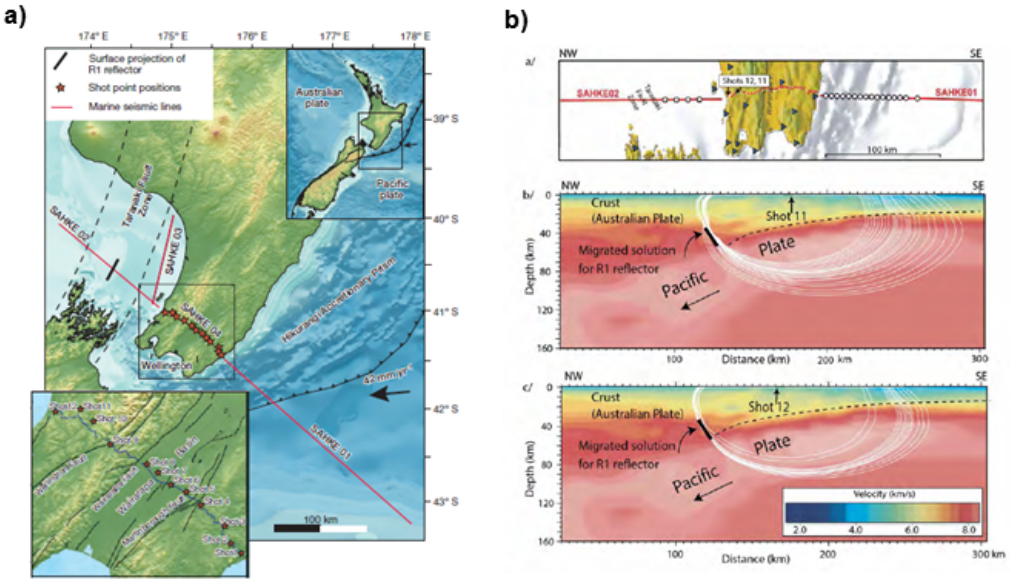

Fig. 4: Figure illustrating the location and velocity models created by Stern et al. a) illustrates the location of the shot points in New Zealand. The direction of oblique subduction of the Pacific plate beneath the Australian plate is shown by the black arrow; top insert shows the plate tectonic setting of New Zealand; bottom inset shows enlarged section showing seismograph lines and shot positions, and the mapped faults crossed by the seismic line are labelled. b) illustrating a the top: plan view of onshore and offshore shot lines; mid and bottom: results of velocity models created by 3-D tomography to carry out a migration of reflecting picks for two different shots respectively, from Stern et al. (2015).

2 Method

2.1 Introduction

There are at least three important steps in computational modelling of any physical process: i) the problem definition, ii) the choice of a mathematical model and iii) the computer simulations.

This work started defining an idealization of the problem of interest: " Does a weak layer at the base of an oceanic plate play any role on subduction dynamics?". This was followed by the definition of a set of relevant physical quantities chosen to be tested or measured (full scheme is available in tab. 2). In numerical modelling, it might not always be possible to guarantee the fidelity of the idealization, since the physical process is not totally understood (e.g., the case of a complex environment within the deep Earth structure where obtaining direct measurements is difficult, if isn't impossible).

The second step of the modelling process is to represent an idealization of the physical reality by a mathematical model: the governing equations of the problem. These are available in fluid dynamics for the Navier–Stokes problem which is the case examined. The Navier–Stokes equations are considered to be an accurate representation of the fluid motion. However, it's needed to introduce simplifying assumptions to reduce the complexity of the mathematical model and make it amenable to either exact or numerical solution (see also sections 2.2 and 2.2.2).

After the selection of an appropriate mathematical model, together with suitable initial and boundary conditions (see section 2.4), it's possible to proceed to its solution (Peiró and Sherwin, 2005).

The chapter start by briefly introducing the concept of conservation laws and their differential representation as PDEs and alternative forms. Follow, by the classification of the constitutive visco-plastic laws used in the thesis. The classification of these equations is important, since a rheological model is fundamental in solving the system of conservation equations. Then, by presenting the numerical codes used in this thesis to derive such equations and performing computer simulations: MVEP2 (Crameri and Kaus, 2010) and LaMEM (Kaus et al., 2015), and associated model boundary conditions. LaMEM (Lithosphere and Mantle Evolution Model) is a 3-D parallel, finite difference staggered grid code and MVEP2 is a 2-D finite element code. The chapter concludes by description of the model set-up and with a list of the

variables and parameters investigated during this thesis work.

2.2 Governing equations

In geodynamics, a continuum mechanics approximation is widely used to describe geological and geophysical processes. These processes are defined by a set of balance equations, the conservation equations together with the constitutive relationship. Therefore the mayor rock units, such as the Earth's crust and mantle, are consider as a continuous geological media and the conservation equations are based on the general continuum hypothesis.

Continuity of any medium implies that, on a microscopic scale, the material under consideration doesn't contain mass-free voids or gaps (if pores cavities are present they are indeed filled with some continuous substances). As the different properties of a continuum may vary at every geometrical point, then a continuous description is needed. These hypotheses can describe the physic of a fluids behaviour, as well as the nature of an elastic media as fit very well ordinary fluids at the laboratory scale.

Since the mantle behaves basically like a viscous fluid over a geological time scale (see section, 2.2.2), then the same hypothesis are used for the mantle. Despite the fact that the mantle it's known to be heterogeneous at various scale and made of compositional distinct grains (Ricard, 2007). The basic conservations laws are below briefly summarised. For further details see Ismail-Zadeh and Tackley (2010); Ricard (2007); Turcotte and Schubert (2014).

2.2.1 Conservation equations

The conservation equations consist in a set of balance equations for mass, momentum and energy. In this thesis the Stokes equations are only solved for the conservation of mass and momentum, assuming incompressibility and neglecting temperature.

2.2.1.1 Conservation of mass The conservation of mass during the displacement of a continuous medium is described by the continuity equation. The mass conservation equation, like many other time-dependent conservation equations, can be either Eulerian or Lagrangian depending on the nature of a geometrical point of observation for which the equation is written.

From Ricard (2007), the Eulerian form of the mass conservation relationship is:

$$\frac{\partial \rho}{\partial t} + \boldsymbol{\nabla} \cdot (\rho \mathbf{v}) = 0 \tag{1}$$

The equations (1) establish the mass balance within an elementary volume during the displacement of continuous medium. Where ρ is the density (the amount of mass per unit of volume), $\mathbf{v}$ is the local velocity vector of a material and $\rho\mathbf{v}$ is the mass flux.

For a case of an incompressible fluid, in the Lagrangian reference frame, particles have constant density therefore the Lagrangian observer doesn't see any density variation and $D\rho/Dt = 0$. When pressure and temperature changes are not very large and no phase transformations lead to volume changes occur in the medium, the mass conservation equation is called continuity equation and becomes:

$$\boldsymbol{\nabla} \cdot \mathbf{v} = 0 \tag{2}$$

from Ricard (2007). The incompressible form of the mass conservation equation is broadly used in numerical geodynamic modelling, although in many cases it is rather big simplifications (e.g. case of the whole mantle convection, Tackley (2008).

2.2.1.2 Conservation of momentum The momentum equation is a differential equivalent to the famous Newton's second law of motion ($\mathbf{f} = m\mathbf{a}$). The rate of change of the momentum of a material in a volume Ω is related to the body forces acting in the volume Ω and to the surface forces acting on its surface Σ. The general expression for linear momentum is:

$$\int_{\Omega} \rho \mathbf{v} \, dV, \tag{3}$$

The total momentum variations are due to:

1. adjective transport of momentum across the surface Σ;
2. forces acting on this surface;
3. internal body forces.

fromRicard (2007). The balance of the various internal and external forces acting on a continuous body determine its deformation. The conservation of momentum for a continuous medium in the gravity field relates forces

and deformation. From Gerya (2009), in the Eulerian reference frame it can be expressed as follow:

$$\frac{\partial \sigma_{ij}}{\partial x_j} + \rho g_i = \rho \left(\frac{\partial v_i}{\partial t} + v_j \frac{\partial v_i}{\partial x_j} \right), \tag{4}$$

Where i, j represent spatial directions and follow the Einstein summation convention, ρ is the fluid density, g_i is the gravitational acceleration, v_i is the velocity, and x_j is the spatial coordinate.

The relationship of the total stress tensor introduces pressure into the momentum equation:

$$\sigma_{ij} = -P\delta_{ij} + \tau_{ij} \tag{5}$$

where total stress field σ_{ij} is subdivided into a static part $P = -\sigma_{kk}/3$ (thermodynamic pressure, which exists even if the fluid is at rest), and a dynamic part τ_{ij}. δ_{ij} is the Kronecker's delta which equals 1 if $i = j$ and 0 if $i \neq j$.

One can obtain the Navier-Stokes equation of motion using the moment equation (4) and the relationship of the total stress tensor (5), as:

$$\frac{\partial \tau_{ij}}{\partial x_j} - \frac{\partial P}{\partial x_i} + \rho g_i = \rho \frac{Dv_i}{Dt}. \tag{6}$$

where $\frac{Dv_i}{Dt}$ is the substantive time derivative of the velocity vector.

As rocks behave as a highly viscous fluid on the geological time scale, therefore in the equation (6), the right-hand-side term can be neglected obtaining the following Stokes equation:

$$\frac{\partial \tau_{ij}}{\partial x_j} - \frac{\partial P}{\partial x_i} + \rho g_i = 0. \tag{7}$$

The Stokes equation is solved for pressure and velocity. When the components of the deviatoric stress tensor (τ_{ij}) are calculated using the newtonian constitutive relationship between the stress and strain rate, the equation above (7) can be further simplified as:

$$\eta \frac{\partial^2 v_i}{\partial x_j^2} - \frac{\partial P}{\partial x_i} + \rho g_i = 0. \tag{8}$$

For more details, see section 2.2.2.1.

2.2.2 Constitutive equations: rheology laws

In rheology, an equation which relates kinematic quantities (such as displacement, velocity, deformation and fluxes) to dynamic quantities (forces and stresses) is called a constitutive relationship.

Rheology is defined as the study of deformations and flow of matter. The constitutive equations are essential for solving the conservation equations, as they define the intrinsic properties of matter determining its behaviour (Malkin et al., 2006).

Matter can behave either elastically, viscously or plastically or in a combination of them (see fig. 5).

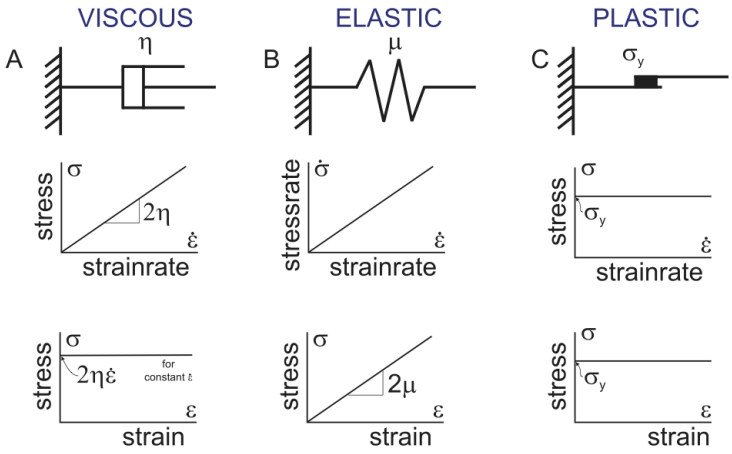

Fig. 5: Figure illustrates the viscous, plastic and elastic basic deformation behaviour. Mechanical equivalent (top), stress/strainrate or stressrate/strainrate response (middle) and stress/strain behaviour under constant strainrate conditions (bottom), from Kaus (2014).

On a short time scale (seconds), Earth appears static and any deformations are reasonably well described using an elastic rheology (e.g earthquakes). On geologically larger time scales (millions to billions of years), the Earth mantle acts basically like a (very viscous) fluid and viscous rheology defines its mechanical behaviour. Lastly, the mechanism of plastic deformation describes the effect of rocks having a finite strength; when differential stresses are larger than a given value (yield-stress), rocks will fail. Plasticity is typically found in the form of faults or shear-zones.
The Maxwell time controls the relative importance of elastic and viscous behaviour. Therefore, it's the ratio between viscosity η and shear modulus

G:

$$\tau_M = \frac{\eta}{G} \tag{9}$$

Materials deform mainly in a viscous way for a time larger than the Maxwell time. The geological processes related to the mantle convection have classically a characteristic time of 10 Myrs, for a typical values of viscosity and shear modulus of $\eta \approx 10^{21}$ $[Pa \cdot s]$ and $G \approx 10^{11}$, respectively. For more details see Ricard (2007).

The mantle has a relatively small Maxwell time, therefore it basically behaves as a viscous fluid on geological time scales. The characteristic time for the lithosphere is, instead, much larger, and elasticity shouldn't be ignored. Elastic and viscous deformations can also occur simultaneously.

Materials strength is also very dependent on temperature, pressure and rock composition. All of these factors can change greatly studying the inside of planets. Despite all the efforts, rheology still remains poorly known parameter in solving the dynamics of the Earth's interior.

2.2.2.1 Visco-Plastic rheology The visco-plastic rheology used in this thesis employs plastic (brittle) deformation conditions under/near the surface and newtonian viscous (ductile) conditions into the mantle. The visco-plastic rheology relationship when written in tensorial form assume the form:

$$\dot{\varepsilon} = \dot{\varepsilon}_{ij}^{\mathrm{vs}} + \dot{\varepsilon}_{ij}^{\mathrm{pl}} = \frac{1}{2\eta}\tau_{ij} + \dot{\lambda}\frac{\partial Q}{\partial \sigma_{ij}}. \tag{10}$$

$\dot{\varepsilon}_{ij}^{\mathrm{vs}}$ and $\dot{\varepsilon}_{ij}^{\mathrm{pl}}$ are the viscous and plastic strain rate components respectively. Q is the potential plastic flow and $\dot{\lambda}$ is a plastic multiplier. A visco-plastic rheology implies plastic body behaviour under large differential stresses and viscous body behaviour under long time scales.

In the following sub paragraph the linear and plastic constitutive laws are explored in more detail.

Linear or Newtonian viscous deformation The Linear or Newtonian viscous type of deformation is applied to the mantle rocks modelled in this thesis.

The relationship between the stress and strain rate defining this mode of deformation, is described by taking into account the total stress relationship

σ_{ij} in equation (5) and linearly relating the deviatoric stress τ_{ij} to the rate of deformation, or strain rate, $\dot{\varepsilon}_{ij}$. As it shown in the following steps:

$$\tau_{ij} = \lambda' \dot{\varepsilon}_{kk} \delta_{ij} + 2\eta \dot{\varepsilon}_{ij}. \tag{11}$$

where λ' is the bulk viscosity and η is the shear viscosity. The strainrate is defined as:

$$\dot{\varepsilon}_{ij} = \frac{1}{2}\left(\frac{\partial v_i}{\partial x_j} + \frac{\partial v_j}{\partial x_i}\right) \tag{12}$$

where v_i is the fluid velocity vector. The strainrate $\dot{\varepsilon}_{ij}$ is usually split in an isotropic and deviatoric part, as follow:

$$\dot{\varepsilon}'_{ij} = \dot{\varepsilon}_{ij} - \frac{1}{3}\dot{\varepsilon}_{kk}\delta_{ij} \tag{13}$$

In geodynamic applications, incompressibility is normally assumed, i.e. $\dot{\varepsilon}'_{kk} = \boldsymbol{\nabla} \cdot \mathbf{v} = 0$. In this case, or in the case of an incompressible fluid with linear Newtonian rheology, the stress and strain rate become:

$$\tau_{ij} = 2\eta \dot{\varepsilon}^{vis}_{ij} \tag{14}$$

or

$$\dot{\varepsilon}^{\text{vis}}_{ij} = \frac{1}{2\eta}\tau_{ij}, \tag{15}$$

from which the definition of viscosity follows:

$$\eta = \frac{\tau_{ij}}{2\dot{\varepsilon}^{vis}_{ij}} \tag{16}$$

for any i and j.

In a viscous rheology η is independent of the state of stress, but it is usually strongly dependent on other factors, such as temperature, grain size, confining pressure and fluid content (not take into account in this thesis, see also section 4.3).

Plastic rheology Plastic rheology describes the relationship between stress and deformation that leads to a permanent deformation of the media (also known as a non-recoverable strain). This occurs in rocks when they are subjected to differential stresses larger than a yield-stress and fail. Plasticity

is typically found in the form of faults or shear-zones (i.e., if the fault doesn't rupture (to generate an earthquake) then the surrounding ground may become permanently distorted (e.g. a shear zone).

The so called Byerlee's law describes the maximum strength of the upper crustal rocks which increases with rising in confining pressure (depth). It was obtained from a large number of laboratory experiments performed on various rocks types.

The depth-dependent strength of crustal rocks is often represented by the Mohr-Coulomb yield function. This can be written as:

$$F = \tau^* + \sigma_{\mathrm{N}} \sin(\phi) - C\cos(\phi) \tag{17}$$

with $\tau^* = (\frac{\sigma_1 - \sigma_3}{2})$ and $\sigma_{\mathrm{N}} = (\frac{\sigma_1 + \sigma_3}{2})$. C is the rock cohesion (typically 20-50 MPa) and (ϕ) is the internal friction angle (generally 30-50°). If F<0, stresses are too low for plastic yielding to occur. If stresses are sufficiently large, plastic deformation is activated. Plasticity relationship is given by:

$$\dot{\varepsilon}_{ij}^{\mathrm{pl}} = \dot{\lambda}\frac{\partial Q}{\partial \sigma_{ij}} \tag{18}$$

where Q is the plastic flow potential and is given by:

$$Q = \tau^* + \sigma_N \sin(\psi) \tag{19}$$

where ψ is the dilatation angle (i.e. it indicates how much a fault zone "expands" during deformation), which is typically <10°. Furthermore, the determination of $\dot{\lambda}$ ensures that F=0. Mathematically, this is done by the Karush-Kuhn-Tucker condition:

$$\dot{\lambda}F = 0, \dot{\lambda} \geq 0, F \leq 0 \tag{20}$$

From Kaus (2014).

2.3 Numerical codes

The two computational codes MVEP2 and LaMEM were used to perform the computer simulations show in section 3 and 5. The two codes numerically solve the governing equations defined in section 2.2.1. The major difference between the two numerical codes is the technique used to solve the partial differential equations: MVEP2 is based on the finite element

method (FEM) whereas LaMEM in based on the finite difference method (FDM). The FDM is the oldest numerical technique developed to approximate the differential equations (PDE's) and is based on the application of a local Taylor expansion series to approximate the PDEs. Subsequently, additionally techniques were developed, for example the finite element method. All these methods have some similarities. However, there are relative advantages and disadvantages in each approach. For further details see for example Peiró and Sherwin (2005). In this section, the description of how a numerical solution is obtained is not discussed, as it can be found in several finite difference and finite element methods's text books, see Strang and Fix (1973); Zienkiewicz and Taylor (2000); Gerya (2009). Further details about the two numerical codes are also given in the respective subsection, 2.3.1 and 2.3.2.

2.3.1 MVEP2

A part of the simulations performed in this thesis and shown in appendix A were computed using MVEP2, which is the latest version of MILAMIN_VEP2 (Crameri and Kaus, 2010). MVEP2 is a 2-D Lagrangian thermo–mechanical finite element code, combined with a marker and cell approach to simulate geodynamic processes. The advection of the parameters is done by deforming the Lagrangian mesh. This code was used in order to solve for linear viscous deformation of a weak layer at the base of an oceanic plate in a contest of dynamic subduction, the model setup is shown in section appendix A. One of the main advantages of the code is that it is relatively easy to setup models, change the rheology, visualize results and perform productive runs. Despite being written in MATLAB and being based on direct solvers, the code is relatively efficient thanks to the use of fast matrix assembly routines and MUTILS. It can use both quadrilateral (structured) meshes (with quadratic or linear elements) or unstructured triangular meshes. In this thesis a quadrilateral type element was used, see fig. 6.

2.3.1.1 Mathematical approach MVEP2 is based on finite element method which is a technique for solving partial differential equations. The process of obtaining a computational solution consists of two stages. The first stage converts the continuous partial differential equation and auxiliary (boundary and initial) conditions into a discrete system of algebraic equations. This first stage is called discretisation. It is carried out locally over small

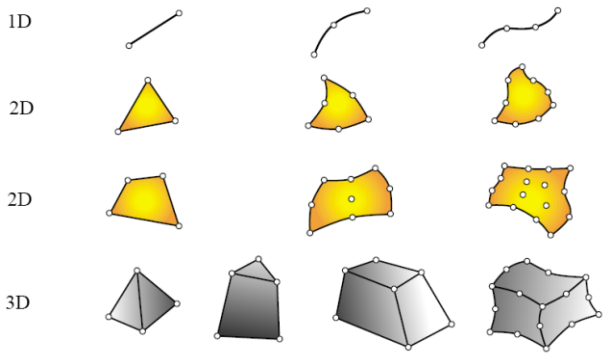

Fig. 6: Figure showing the finite elements, from Kaus (2014).

regions of simple but arbitrary shaped elements, the finite elements (fig. 6).

This process results is a matrix who connects load at the nodes of the element with output at the same points. The second stage involves solving the system of algebraic equations to obtain an approximate solution to the original differential equation. The solution is approximate since errors are introduced by the replacement of continuous differential terms in the governing partial differential equation by algebraic expressions connecting nodal values on a finite grid. The approximation of the continuous variable is made in terms of nodal variables using shapes functions. The choice of a shape function is directly related to the choice of an element type.

For solving the equation over larger regions, one sums node-by-node the matrix of equations for the smaller sub-regions (elements) resulting in a global matrix equation. This system of equations can then be solved simultaneously by standard linear algebra techniques to yield nodal displacements. This last step completes the numerical solution of the differential equation.

The complete discretised Stokes problem (on the element level) can be compactly expressed as:

$$\begin{bmatrix} \mathbf{K}^e & \mathbf{G}^e \\ (\mathbf{G}^e)^T & \mathbf{0} \end{bmatrix} \begin{bmatrix} \mathbf{U}^e \\ \mathbf{p}^e \end{bmatrix} = \begin{bmatrix} \mathbf{f}^e \\ \mathbf{0} \end{bmatrix}$$

where

$$\mathbf{K}^e = \int_{\Omega^e} \hat{\mathbf{B}}^T \mathbf{D} \hat{\mathbf{B}} dV,$$

$$\mathbf{G}^e = -\int_{\Omega^e} \hat{\mathbf{B}}^T \mathbf{m} \mathbf{N}_p dV,$$

where $\mathbf{U}$ and $\mathbf{p}$ are the velocity and pressure vectors respectively, and

$$\mathbf{f}^e = \int_{\Omega^e} \begin{bmatrix} \mathbf{N}^T & f_x \\ \mathbf{N}^T & f_y \end{bmatrix} dV - \oint_{\Gamma^e} \begin{bmatrix} \mathbf{N}^T & t_x \\ \mathbf{N}^T & t_y \end{bmatrix} dS$$

for more details, see e.g. Kaus (2014).

2.3.2 LaMEM

LaMEM was used to perform 2-D and 3-D high resolution simulations for linear and non-linear rheology shown in section 3. LaMEM (Lithosphere and Mantle Evolution Model) (Kaus et al., 2015) is a 3–D parallel, finite difference staggered grid code. In the 3-D Cartesian domain a Lagrangian particle-in-cell method is used for accurately tracking distinct material domains as they undergo extensive deformation due to creeping flow. The code is written in C and uses the PETSc library. The code is currently under development for an open-source release since 2016.

2.3.2.1 Mathematical approach The conservation equations are discretized in space using a staggered grid finite difference scheme, for more details see Harlow and Welch (1965). A low-order, stable discretization FD scheme is used for an incompressible fluid flow. For the grid layout see fig. 7. To achieve scalability distributed arrays (DMDA) and iterative solvers (KSP, SNES) are used, from the PETSc library.

A Marker And Cell (MAC) method (Harlow and Welch, 1965) tracks material properties and implement material advection in an Eulerian kinematical framework. To prevent spurious clustering of the material particles (markers) a combination of a fourth–order Runge–Kutta method with a conservative velocity interpolation is used. During the advection, the history stresses from previous time step (τ_{ij}^n) are corrected on the markers to account for the rigid-body rotation, and then interpolated on the edge and cell control volumes (fig. 7) using the distance–based averaging algorithm to obtain the effective strain rates, $\dot{\varepsilon}_{ij}^*$:

$$\dot{\varepsilon}_{ij}^* = \dot{\varepsilon}_{ij} + \frac{\tau_{ij}^*}{2G\Delta t}, \tag{21}$$

$$\tau_{ij}^* = \tau_{ij}^n + \Delta t(w_{ik}\tau_{kj}^n - \tau_{ik}^n w_{kj}) \tag{22}$$

where $\dot{\varepsilon}_{ij} = \frac{1}{2}\left(\frac{\partial v_i}{\partial x_j} + \frac{\partial v_j}{\partial x_i}\right) - \frac{1}{3}\frac{\partial v_k}{\partial x_k}\delta_{ij}$, is the deviatoric strain rate tensor,

$w_{ij} = \frac{1}{2}\left(\frac{\partial v_i}{\partial x_j} - \frac{\partial v_j}{\partial x_i}\right)$ is the spin tensor and G is the elastic shear modulus, (Kaus et al., 2015).

The second invariant of the effective strain rate is computed by cross –interpolation and averaging of the missing data (squares of the corresponding components) between all the control volumes. The effective viscosity (η^*) and the updated deviatoric stresses (τ_{ij}) are computed from the effective strain rates, using the standard quasi-viscous expression:

$$\tau_{ij} = 2\eta^* \dot{\varepsilon}^*_{ij}, \tag{23}$$

$$\eta^* = min\left[\left(\frac{1}{G\Delta t} + \frac{1}{\eta_{vis}}\right)^{-1}, \frac{\tau_Y}{2\dot{\varepsilon}^*_{II}}\right] \tag{24}$$

where τ_Y is the yield stress, which is determined by enforcing the Drucker-Prager yield criterion:

$$\tau_{II} \leq \tau_Y = \sin(\phi)p + \cos(\phi)c \tag{25}$$

where $\tau_{\mathrm{II}} = \left(\frac{1}{2}\tau_{ij}\tau_{ij}\right)^{(1/2)}$, ϕ is the friction angle and c is the cohesion, from Kaus et al. (2015).

2.4 Boundary conditions

The boundary conditions are necessary in order to solve PDE's equations and determine the intrinsic behaviour of the model. One must define a set of boundary conditions applicable to the fundamental equations and specific for the geodynamic problem investigated.

All the boundaries of the models shown in this thesis have a free slip condition expect for the models shown in section 3.2.6, which have a free surface boundary condition at the top boundary. Temperature evolution is, instead, ignored in all the models.

A free slip condition indicates that all the velocities orthogonal to the boundary are equal to zero. The gradients of the other two components are also assumed to vanish. This implies zero shear strain rate and shear stress along the boundary. For example, for the boundary orthogonal to the x

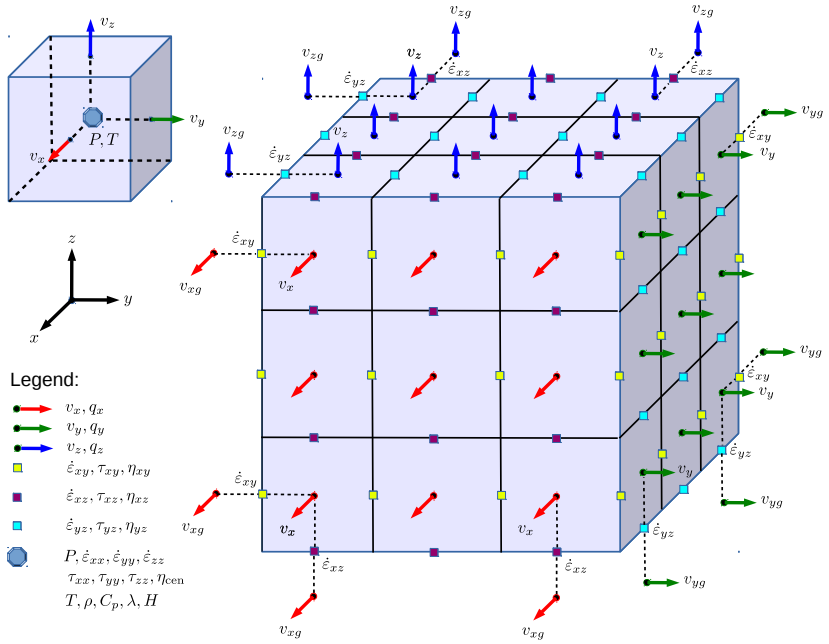

Fig. 7: Figure showing the finite difference staggered grid approach, illustrating the ordering of the variables, from Kaus et al. (2015)

axis, the free slip boundary condition is explicated as:

$$v_x = 0, \tag{26}$$

$$\frac{\partial v_y}{\partial x} = \frac{\partial v_z}{\partial x} = 0 \tag{27}$$

A free surface condition requires both shear and normal stress at the boundary to be zero, as follow:

$$\sigma_{\mathrm{ij}} = 0 \tag{28}$$

In LaMEM, the free surface is implemented using a so-called sticky air approach, which assigns a relatively low but non-zero viscosity to the air phase, together with an appropriate stabilization method allowing sufficiently large time steps. The topography of the free surface is explicitly tracked by an internal 2-D grid that covers the entire domain. Then, a 40 km thick "sticky air" layer ($\rho_{\mathrm{air}} = 1[kg/m^3]$ and $\eta = 10^{18}[Pa \cdot s]$) was used in order to mimic the effect of a free surface and stabilise the development of the topography.

2.5 Model setup

The initial model setup was built from the benchmark paper of Schmeling et al. (2008) as shown in section 3.2.6. The model setup was adapted to solve the problem studied in this thesis taking into account the numerical limitations of the code (see Appendix A).

Fig. 8 shows the setup for the pseudo-2D and 3-D models developed and used in this thesis. The pseudo 2-D and 3-D models were performed with a resolution of 512x128x2 and 512x28x128, respectively. All the phases are incompressible and can be modelled as linear viscous expect for the crust which has a visco-plastic rheology. The visco-plastic rheology of the crust has facilitated the development of a weak hinge zone promoting the decoupling of the plates from the upper surface of the model and it descends into the mantle.

Subduction is dynamically initiated by forcing the sinking of the oceanic plate into the mantle. The initial conditions for the subducting plate include a slab tip already penetrating into the mantle, 257 km deep with a dip angle of 34 ° to the horizontal. A similar geometry setup was also explored in an analogous computer simulations (Enns et al. (2005); Stegman et al. (2006) and Schellart et al. (2007)).

The modelled weak layer is located at the base of the oceanic plate and has the same x and y dimensions of the oceanic plate. As the WL thickness was shown to not play a main role in the subduction processes up to a value of 50 km (section 3.2.4) 30 km was selected for the slippery layer thickness. This was also due to the resolution limits encountered using the code.

All the simulations performed were compared with the reference model which does not contain a WL, described in section 3.1. Summarised in fig. 8 and tab. 1 and 2) are the geometrical and physical characteristics of the selected experiments described in the thesis.

The lithosphere-mantle deformation was evaluated by employing a relatively simple numerical model for a convection in a fluid which has a low viscosity layer lying between a rigid lid and a soft mantle. Finite difference/element calculations were used to determine the effects of:

1. viscosity ratio between the mantle and weak layer;
2. the density contrast between the mantle and weak layer;
3. the thickness of WL;
4. a stiffer oceanic plate;
5. a linear viscous rheology with free surface top boundary condition.

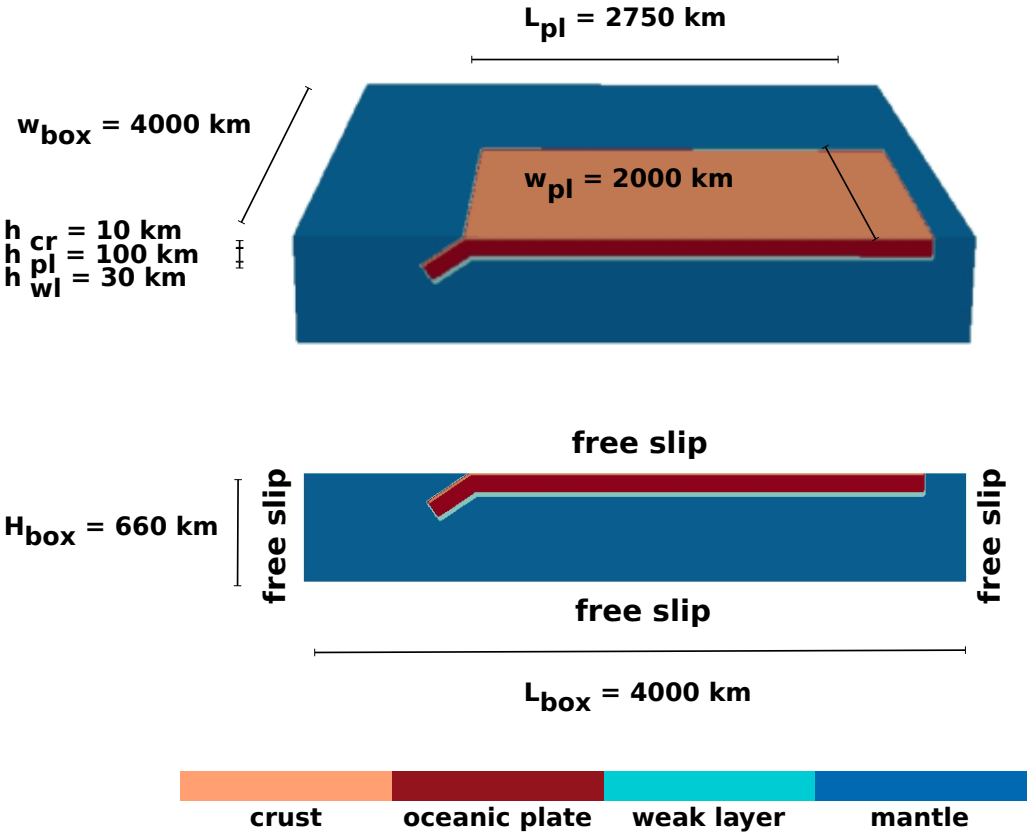

Fig. 8: 3D and 2D model setups. The numerical model domain extends laterally 4000 km in both x and y (for 3D case only) directions and 660 km in the z direction. The oceanic 3D plate geometry was approximated as a rectangular slab extending 2750 km and 2000 km, laterally. The modelled weak layer is located at the base of the oceanic plate and has the same x and y dimensions and a 30 km thickness. The initial geometry consist also in a slab tip already penetrating into the mantle, 257 Km deep with a dip angle of 34 ° to the horizontal.

Symbol	Quantity	**Value**	Units
L_{box}	Domain length	4000	km
H_{box}	Domain height	660	km
W_{box}	Domain width	10-4000*	km
W_{plate}	Plate width	10-2000*	km
L_{plate}	Plate length	2750	km
η_m	Mantle viscosity	2.5×10^{21}	(Pa·s)
η_{crust}	Crust viscosity	2.5×10^{23}	(Pa·s)
ρ_m	Mantle density	3200	kg/m^3
ρ_{crust}	Crust density	3300	kg/m^3
$\Delta\rho_{sm}$	Density contrast slab mantle	100	kg/m^3
g	Gravitational acceleration	10	m/s^2
c	Cohesion	20	10^6 Pa

Table 1: Table illustrating the parameters which were in common to all the simulations performed in this thesis.
* indicates 3-D simulations

Symbol	Quantity	**Reference**	**Range**	Units
η_m/η_{wl}	Viscosity ratio mantle weaklayer	10^0	10^1-10^4	-
η_s/η_m	Viscosity ratio slab mantle	10^2	10^2-10^3	-
$\Delta\rho_{mwl}$	Density contrast mantle weak layer	0	0-200	kg/m^3
h_{wl}	Weak layer thickness	30	10-50	km
h_s	Slab thickness	100	50-150	km
α	friction angle	30	0-30	-

Table 2: Table illustrating the parameters which were varied for the simulations performed in this thesis.
* indicates 3-D simulations

3 Results

The results presented in this chapter aim to constrain the role of a weak layer on subduction dynamics for several important parameters in comparison to the expected subduction regime for the reference model case, for further details see tab. 3. Therefore presented here are the summarised results from a relatively large range of parameters varied, as shown previously in tab. 2. These models explore the control of the weak layer viscosity, density and

Model number	η_m/η_{wl}	$\Delta\rho_{mwl}$	h_{wl}	η_s/η_m	Top BC
RM	10^0	0 kg/m^3	0 km	10^2	free slip
Sim. 1	10^2	0 kg/m^3	30 km	10^2	free slip
Sim. 2	10^3	0 kg/m^3	30 km	10^2	free slip
Sim. 3	10^0	100 kg/m^3	30 km	10^2	free slip
Sim. 4	10^0	200 kg/m^3	30 km	10^2	free slip
Sim. 5	10^2	100 kg/m^3	30 km	10^2	free slip
Sim. 6	10^2	200 kg/m^3	30 km	10^2	free slip
Sim. 7	10^2	0 kg/m^3	10 km	10^2	free slip
Sim. 8	10^2	0 kg/m^3	50 km	10^2	free slip
Sim. 9	10^0	0 kg/m^3	0 km	10^3	free slip
Sim. 10	10^2	0 kg/m^3	30 km	10^3	free slip
Sim. 11	10^0	0 kg/m^3	0 km	10^2	free surface
Sim. 12	10^2	0 kg/m^3	30 km	10^2	free surface
RM*	10^0	0 kg/m^3	0 km	10^2	free slip
Sim. 13*	10^2	0 kg/m^3	30 km	10^2	free slip

Table 3: Table illustrating the simulations shown in this thesis.
* indicates 3-D simulations

thickness on subduction dynamics. Additional simulations which investigate the role of a stiffer oceanic plate and a different top boundary condition are also shown in section 3.2.5 and 3.2.6, respectively.

For a better readability, the acronyms: RM- reference model and Sim.*- where * is the number of the simulation considered, will be used for the rest of the thesis. The lists of parameters that where maintained constant and varied during the simulation are available in tab. 1 and 2, respectively.

In the following paragraphs, the temporal evolution of the subduction models are described based on the differences developed within the three typical temporal evolution stages that all the simulations share in common, namely:

1. an initial period where subduction is dynamically initiated and pro-

gressively accelerates while the slab is sinking into the mantle;
2. an abrupt slab deceleration during its initial interaction with the bottom of the model;
3. a final steady-state configuration at the mid-mantle boundary .

3.1 The reference model

The reference model chosen for the investigation was built, as for the model setup, from a literature benchmark paper of Schmeling et al. (2008) and is shown in fig. 9.

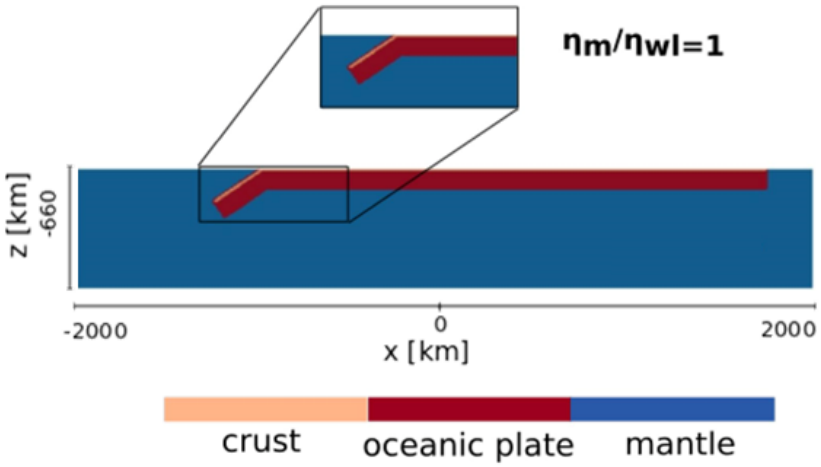

Fig. 9: The subducting plate is 100 km thick, 2000 km wide and 2750 km in length and is covered by a thin crust, 20 km thick. The model employs no WL, and the oceanic plate has a viscosity contrast in the respect to the mantle of 2 orders of magnitude. All modelling box boundaries have a free slip condition.

The reference model and the model setup are identical in respect to all the physical characteristics except for the lack of a weak layer at the LAB, for the case of the reference model. The three typical stages in the temporal evolution of the reference model can be observed in fig. 10 a, b and c. The time evolution of the reference model is presented through the material phase field (fig. 10 a, b and c), velocity field (fig. 10 d, e and f) and deformation flow (fig. 17, a, b and c). The total subduction velocity, slab sinking velocity, horizontal plate velocity, lateral velocity, and the trench velocity will be refereed as V_{total},V_{slab}, V_{plate}, $V_{lateral}$ and V_{trench}, respectively.

0-40 Myr The first temporal evolution stage starts with the initiation of subduction. The leading edge of the lithosphere is forced inside the mantle

with a dip angle of 34° allowing to obtain enough slab pull to be able to overcome the resistance at the trench. The slab approximately reaches a dipping angle value of 60-70° (fig. 10, a) while sinking into the mantle.

During this stage, V_{total} increases progressively, V_{plate} reaches a maximum of 0.7 cm/yr and V_{slab} is approx. 1.1 cm/y (see fig. 10, d). In fig. 11, it is possible to observe an increasing retreating rate for the trench. This stage is always associated with a significant displacement of the mantle from beneath the slab driven by the subducting plate.

40-50 Myr The second phase of the temporal evolution is characterised by the initial interaction of the slab with the bottom of the model. During this stage is observed a slow down in V_{total} with a minimum reached at about 42,5 Myr when slab reaches the bottom of the mid mantle discontinuity (fig. 10,b and e). At this stage, all the components of the velocity field show a characteristic decreasing. However, V_{slab} remains the strongest component of the velocity field $\approx$ 0.8 cm/yr, V_{plate} reaches $\approx$ 0.5 cm/yr and the trench shows a consistent deceleration, see fig. 11.

50-92 Myr The third temporal evolution stage is defined by the sliding of the slab at the bottom of the model (see fig. 10, c). This could be due to the impermeable barrier at the base of the model which can inhibit the flow of the mantle beneath the slab inducing a significant lateral out-of-plane component. The descendent direction of the sinking slab is also more accentuated, see fig. 10, c. During this stage the V_{total} increases again toward an intermediate configuration between the two previous time phases. V_{slab} is approximately 0.9 cm/yr and V_{plate} is roughly 0.7 cm/yr, (fig. 10, f). Characteristic of this stage is the abrupt increase in trench velocity while the slab rolls back, see fig .11.

In 91 Myr, the trench retreats 250 km. The rear edge of the oceanic plate is displaced 575 km starting from its original starting position. The plate average horizontal velocity is 0.631 cm/yr, despite the slab roll back active mechanism.

The physical behaviour of the reference model is consistent with the experimental work performed by Funiciello et al. (2008) and Bellahsen et al. (2005), see also section 4. Since the reliability and the evolution of this model is well known from the literature, it was chosen as a reference base for comparing all the simulations involving the presence of a weak layer at the LAB.

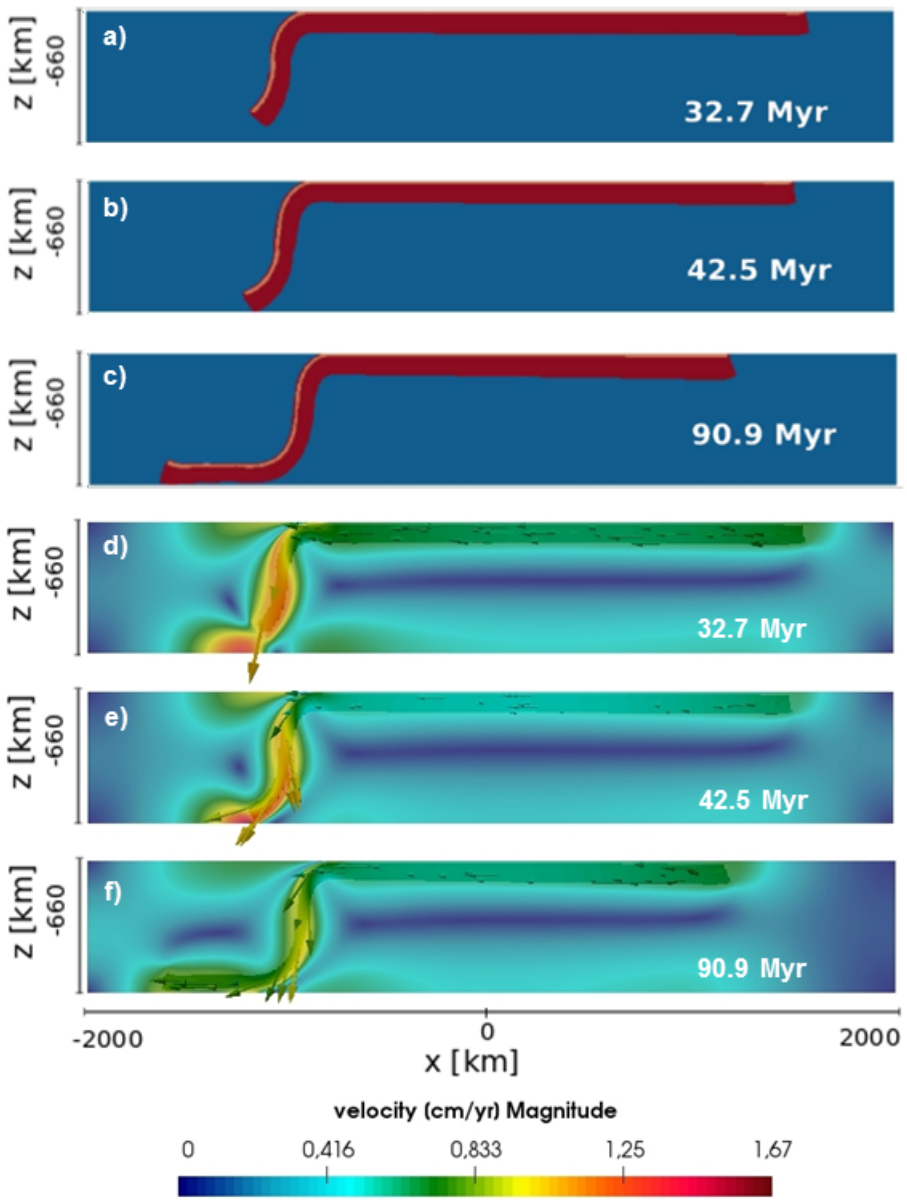

Fig. 10: The phase field and velocity field long term evolution for the RM (with no WL) is represented by a), b), c) and d), e), f), respectively. A final steady state configuration was reached in 90.9 Myr.

3.2 The influence of different parameters

3.2.1 Weak layer viscosity

Simulation 1 has a 2 order magnitude viscosity difference between the mantle and the weak layer, more details are available in tab. 3. This model develops a very dynamic process (see fig. 12). The slab reaches the bottom of the model in 35.5 Myrs which is the fastest time among all models considered and also V_{plate} is higher with respect to the reference model.

0-30 Myr As for the reference model, the fist stage of simulation 1 shows an increase in V_{total} (fig. 12, d). However, the total duration of the stage is shorter and the maximum V_{plate} is reached at approx. 19.8 Myr with a peak velocity of roughly 1.2 cm/yr (fig. 16). Also, in this phase the trench reaches the highest velocity, see fig. 11 .

30-50 Myr For a time bigger than 23 Myr, the sinking of the slab into the mantle generates an abrupt and sharp decrease in V_{total}. The minimum of $V_{plate} \approx 0.8$ cm/yr and $V_{slab} \approx 0.7$ cm/yr are reached when the slab approximates the bottom of the model, in 35.5 Myr, see fig. 12, e). The slab assumes an approx. dip angle of 90°. The WL also seems to progressively escape and uplift from the rear edge of the plate. The trench also undergone an abrupt drop in velocity (fig. 16).

50-92 Myr For a time bigger than 50 Myr, the process evolves into a new configuration. At this stage the V_{plate} shows an intermediate value between the two previous stages ≈1 cm/yr, see fig. 12 and fig. 16.

From fig. 12 (d, e, f), it can be observed that V_{plate} is the highest component of the velocity field during the fist stage of the temporal evolution (d) and V_{slab} is the highest component of the velocity field during the last two phases of the time evolution (e and f). The trench has been displaced forward an backwards over the time, resulting in a quasi-fixed trench position at the final stage, see also fig. 11.

The rear edge of the oceanic plate is displaced 950 km starting from its original position. The plate convergence velocity is in average 1.04 cm/yr, despite a trench quasi stationary active regime.

The fig. 14, shows a comparison between the reference model and simulation 1. For the RM case V_{total} is heterogeneously distributed over the subducting oceanic plate and V_{slab} appears to always be the major velocity

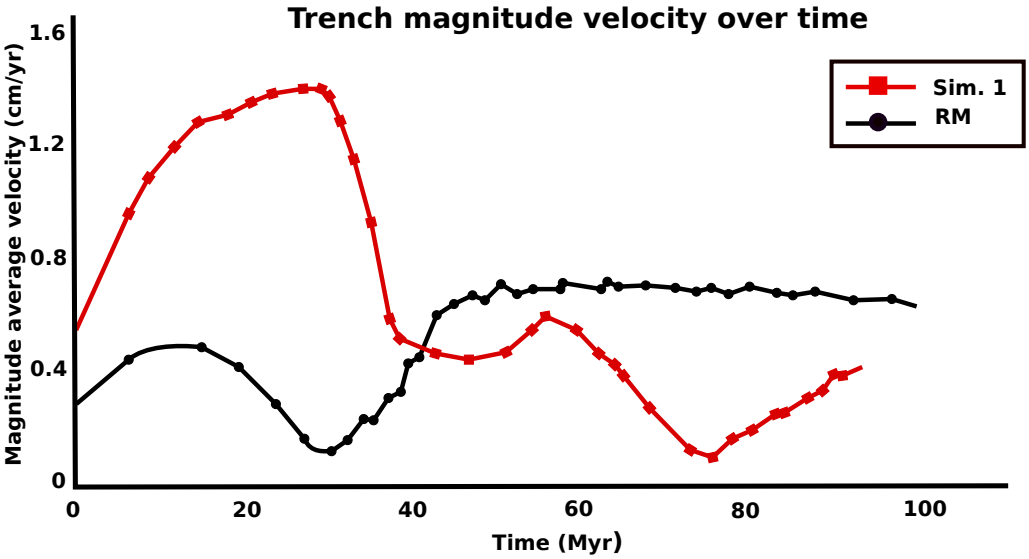

Fig. 11: Comparison of the average trench magnitude velocity over time for the RM and Sim. 1 cases. The time for each simulation was 90.9 Myr and 91.1 Myr respectively.

component.

For Sim. 1, V_{total} varies nearly homogeneously over the subducting oceanic lithosphere during time, without a sharp predominance of V_{slab} over V_{plate} or vice versa over the whole time evolution of the model.

Simulation 2 has a 3 order of magnitude viscosity difference between the mantle and the weak layer, see also tab. 3. This model develops a very distinctive type of subduction. It is characterised by an advancing trench and an overturning of the slab. This simulation shows the highest subduction velocity, despite the slab tip reaching the bottom of the model in 38 Myrs which is an average time between the two previous models.

0-30 Myr The first stage of subduction is similar to the previous models. The subduction initiation is followed by a progressively increasing in V_{total} with time until ca. 20 Myr (see fig. 13, a and d). All the velocity field components increase and the trench advances. The highest velocity is V_{plate} and is developed at the rear plate edge (fig. 13, d).

30-40 Myr Similar to what was seen in the other subduction models, the trend in subduction velocity changes drastically when the slab interacts with the 660 km discontinuity. At this stage, V_{plate} is still the highest velocity while the slab assumes an average dip of about 90° as allowed by the presence of the WL (fig. 13, b) and e). The WL seems to progressively

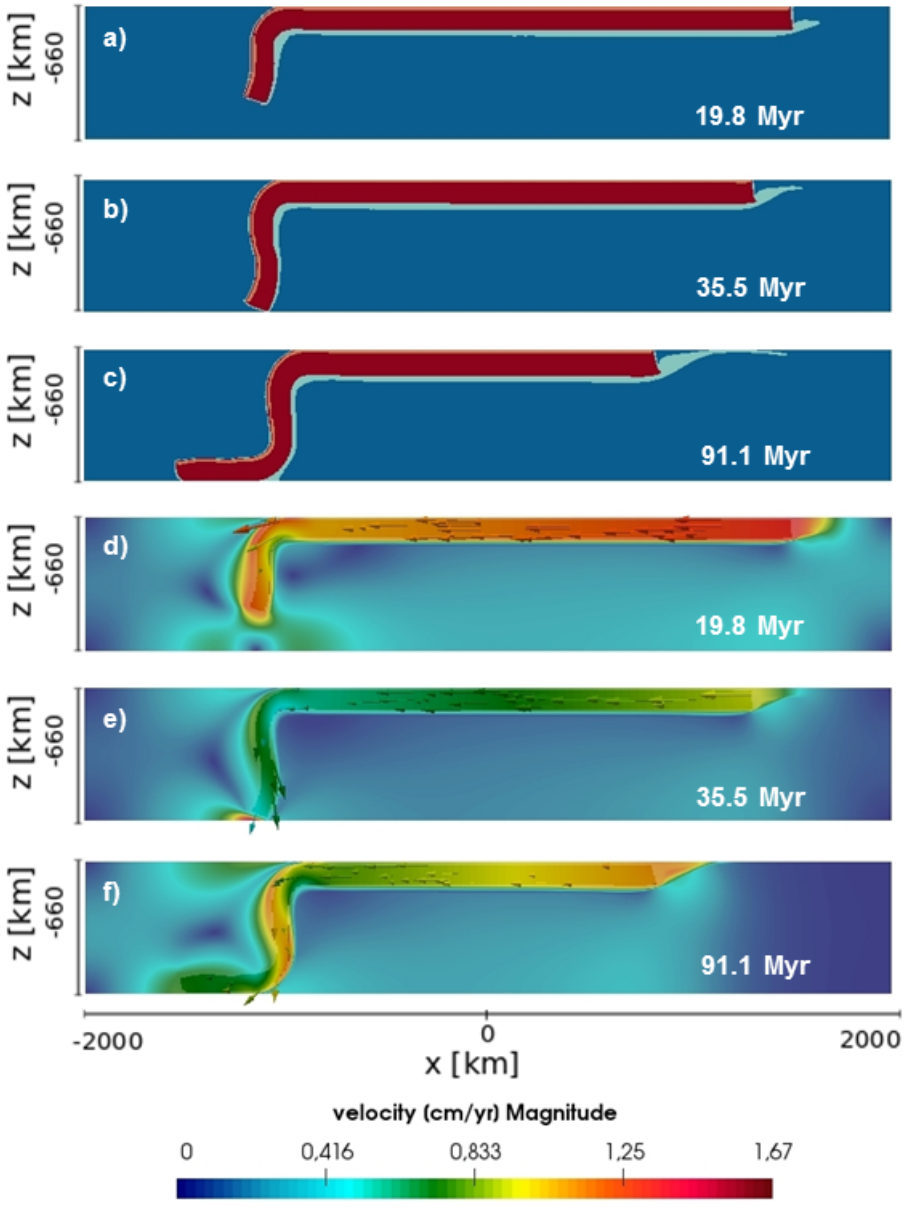

Fig. 12: a), b) & c) represent the phase field development over time for the Sim. 1. d), e) & f) represent the velocity field development over time for Sim. 1. A final steady state configuration was reached in 91.1 Myr.

uplift at the free plate margin (also seen for Sim. 1) and accumulate behind the slab. The slab reaches the bottom of the model at the time of 38 Myr, approx. 5 Myr earlier than seen for the RM case.

40-92 Myr during the third stage, the tip of the slab folds and deforms at depth surpassing the bending resistance. The buckling of the slab is generated by the necessity to overcome the bending resistance and the impermeable barrier at the bottom of the model. Once the resistance at mid-mantle boundary is overcome, the slab motion starts again with a sudden increase in velocity, see fig. 16. The slab bends backwards >90° and the trench rapidly advances. V_{total} is the highest (fig. 13, c and f). As opposed to the previous models where the peak velocity was reached during the first time evolution stage, for. Sim. 3 the peak in plate velocity is reached during this latest stage and is reached on the part of the plate lying at the bottom of the model. The highest V_{plate} is approximately 1.4 cm/yr and is developed in the flat-lying part of the slab.

In 91 Myr, the trench retreats 140 km. The rear edge of the oceanic plate is displaced 1225 km starting from its original starting position. The plate convergence velocity is in average 1.35 cm/yr.

In summary, the RM shows a significantly high slab velocity and a trench retreating mechanism. Sim. 1 shows a higher total subduction velocity with a stronger plate convergence velocity and a quasi-stationary trench mechanism. Sim. 3 shows the highest total subduction velocity developed at the third stage of the temporal evolution with the strongest plate horizontal velocity for an advancing trench and a reverse moving oceanic plate.

Observations In fig. 14 and fig. 15 is shown a comparison between the RM and Sim. 1 and Sim. 2 respectively. From these comparisons, it can be observed that the presence of a low viscosity layer affects the subduction regimes developed during the temporal evolution of the models.

The vertical viscosity structure of the models is also reflected in the evolution of the velocity field. The presence of a weak layer at the LAB influences the subduction velocity, the plate convergence velocity, the slab sinking velocity and trench velocity. A change in the subduction style and in v_{total}, v_{plate}, v_{trench} with the rising in η_m/η_{wl} can also be observed. Additionally, a linear progression can describe the relationships between trench and plate velocity in the models. The fact that simulated trenches are not always

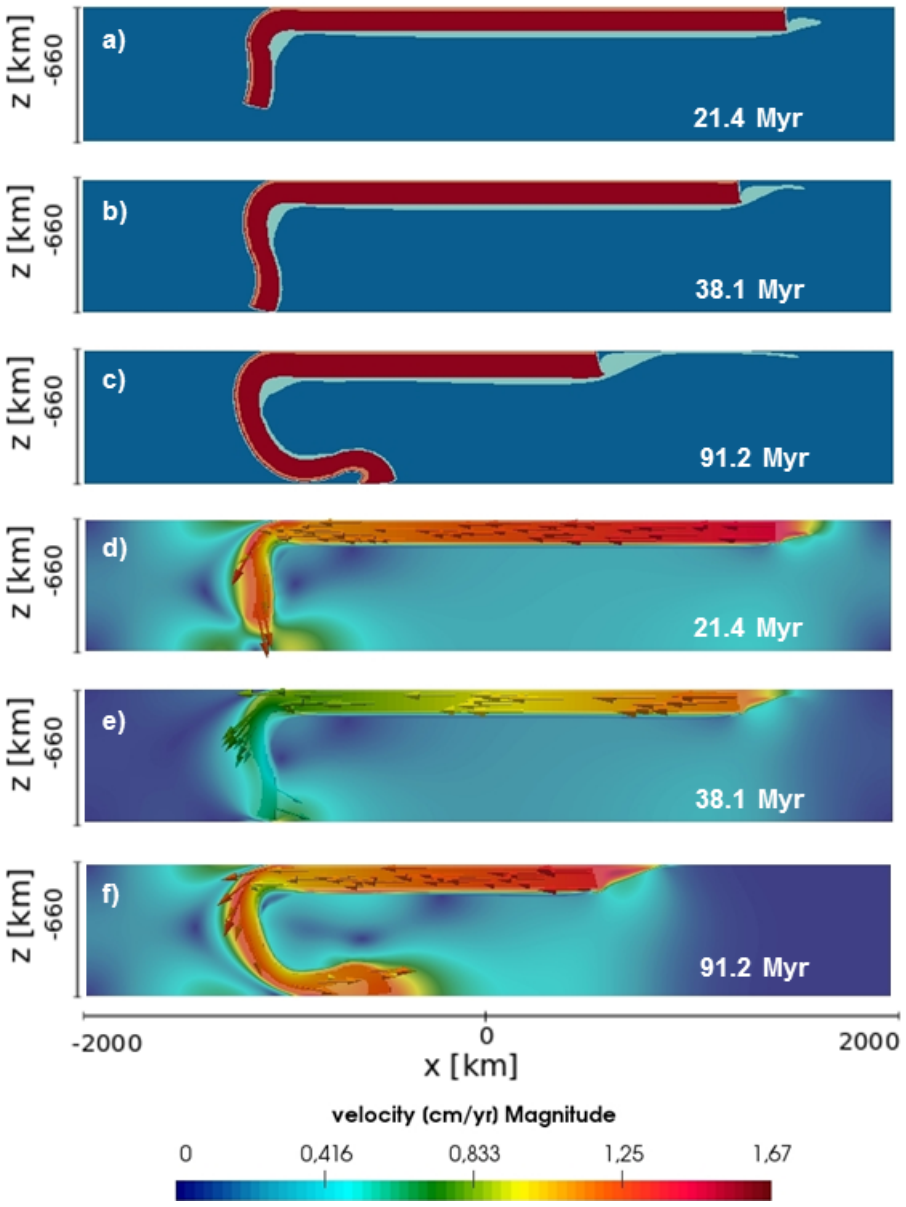

Fig. 13: a), b) & c) represent the phase field development over time for the Sim. 2. d), e) & f) represent the velocity field development over time for Sim. 2. A final steady state configuration was reached in 91.2 Myr

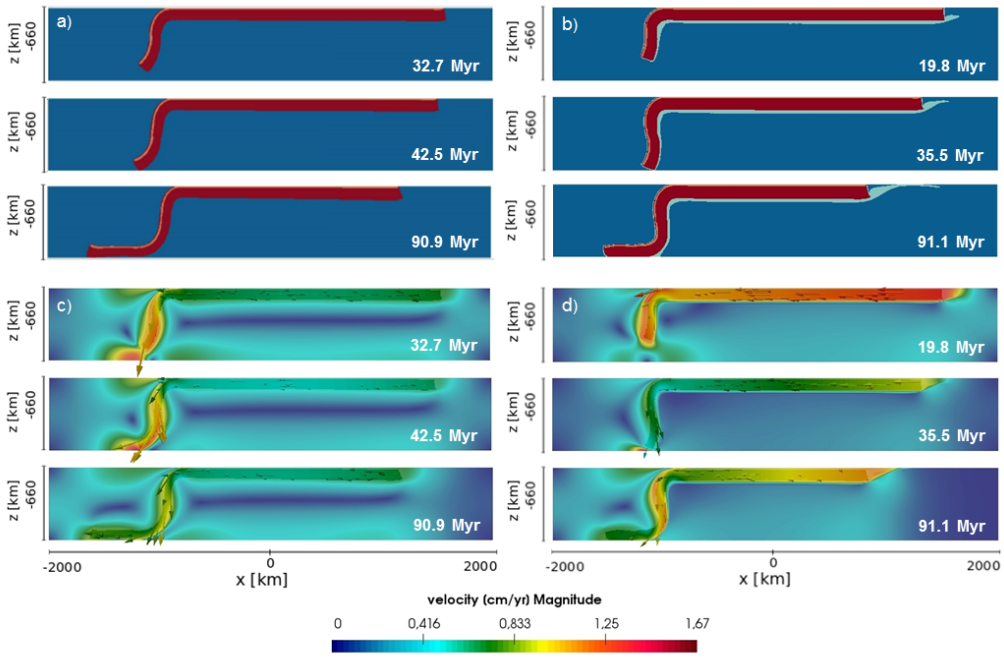

Fig. 14: A comparison between the RM and Sim.1 showing the development of the phase field a), b) and the velocity field c) and d) for each simulation respectively. The time to reach the final steady state configurations for the RM and Sim.1 are 90.9 and 91,1 Myr, respectively.

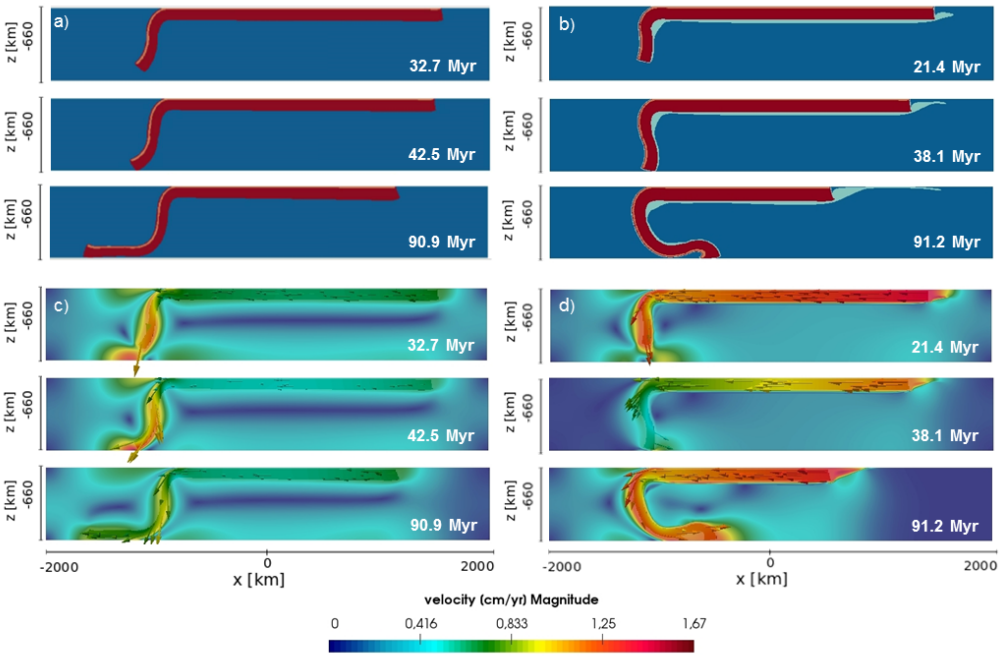

Fig. 15: A comparison between the RM and Sim.2 showing the development of the phase field a), b) and the velocity field c) and d) for each simulation respectively. The time to reach the final steady state configurations for the RM and Sim.2 are 90.9 and 91.2 Myr, respectively.

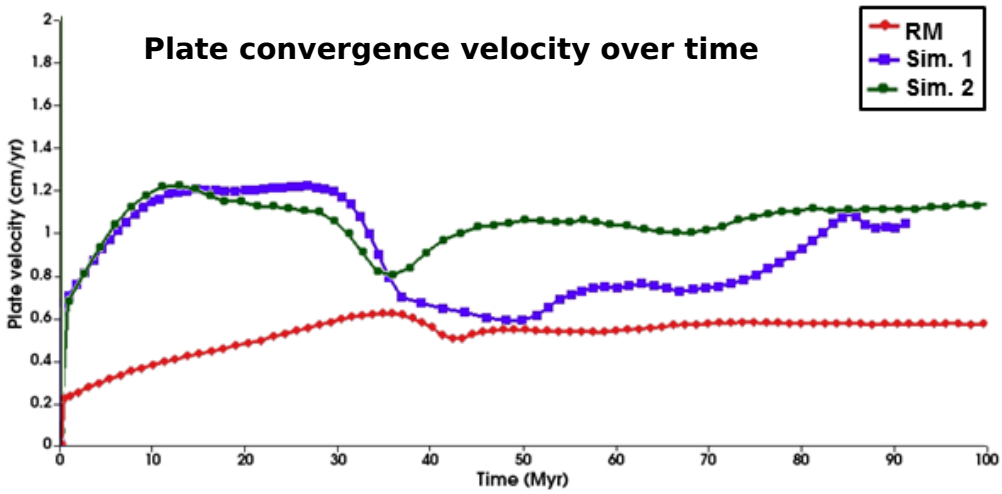

Fig. 16: Comparison of the plate convergence velocity over time for the RM, Sim. 1 and Sim. 2 cases. Sim. 1 and 2 show higher velocities over the time evolution of the models in comparison to the RM.

stationary but indeed move away with respect to the deep anchored slab tip, it could also be enhanced by the presence of a deep impermeable barrier at 660 km depth.

Deformation flow time evolution the simulations performed show the development of the poloidal component of the velocity field. The poloidal flow varies depending on the model, as seen in fig. 17 and described below:

1. RM shows the development of two convective cells;
2. Sim. 1 shows the development of mainly one convective cell, despite during the first stage, a second poloidal flow component was present behind the dipping part of the slab;
3. Sim. 2 shows the development of mainly two convective cells, in which the poloidal flow component behind the dipping part of the slab appears to become progressively predominant.

The progression and intensity of the convective cells seems to relate to the evolution of the subduction velocity field. In fig. 17 a), the RM shows the development of a sharper convective cell in correspondence to the strongest slab velocity developed. For Sim. 1 the development of a second intensive convective cell is observed with the highest plate convergence velocity developed and is located behind the slab, 17 d). Finally, for simulation 3, the

strongest convective cell appears in correspondence to the highest velocity stage 17 i).

3.2.2 Weak layer density

Simulation 3 has a $\eta_m/\eta_{wl} = 1$ and $\Delta\rho_{mwl} = 100$ [kg/m^3]. The morphology of the slab developed during the time evolution (see fig. 18 b) and e)), resembles the one developed for Sim. 1, with a slight increase in the accumulation of the weak layer behind the bending part of the slab. The slab reaches the bottom at an approx. time of 53.0 Myrs and shows a quasi stationary trench mechanism. Sim. 3 develops the subduction mechanism seen for Sim. 1, involving a lower velocity.

Simulation 4 has a $\eta_m/\eta_{wl} = 1$ and $\Delta\rho_{mwl} = 200$ [kg/m^3]. The morphological evolution of the slab is different from Sim 3, as from the second stage of the temporal evolution, an overturning tendency for the slab can be observed with a major accumulation of WL behind its bending part, fig. 18 c). The bottom of the model is reached in 69.0 Myr and at the latest stage the slab overturns and the plate moves backwards while the trench advances. This subduction mechanism is similar to the one observed in Sim. 2 with a minor buckling at the slab tip, see fig. 18 f).

The effect of a light "melted" density channel at the LAB boundary on subduction dynamic can be quickly deduced from a comparison between the RM and Sim. 3 and 4 shown in fig. 18. Both Sim. 3 and Sim. 4 show a lower subduction velocity compared to the previous models.

The density contrast between mantle and weak layer affects the subduction regime and the subduction velocity developed. A linear regression can describe the relationship between v_{total} and $\Delta\rho_{mwl}$.

3.2.3 Coupling weak layer viscosity and density effects

Simulation 5 has a $\eta_m/\eta_{wl} = 10^2$ and $\Delta\rho_{mwl} = 100$ [kg/m^3]. The morphological evolution of this model is similar to those developed in Sim. 2 and 4. The bottom of the model is reached in 44.6 Myr (fig. 19 b)), which is an intermediate time between Sim. 2 and 4. The subduction mechanism developed is characterised by an advancing trench and a reversing plate. The slab tip also shows an incipient folding deformation.

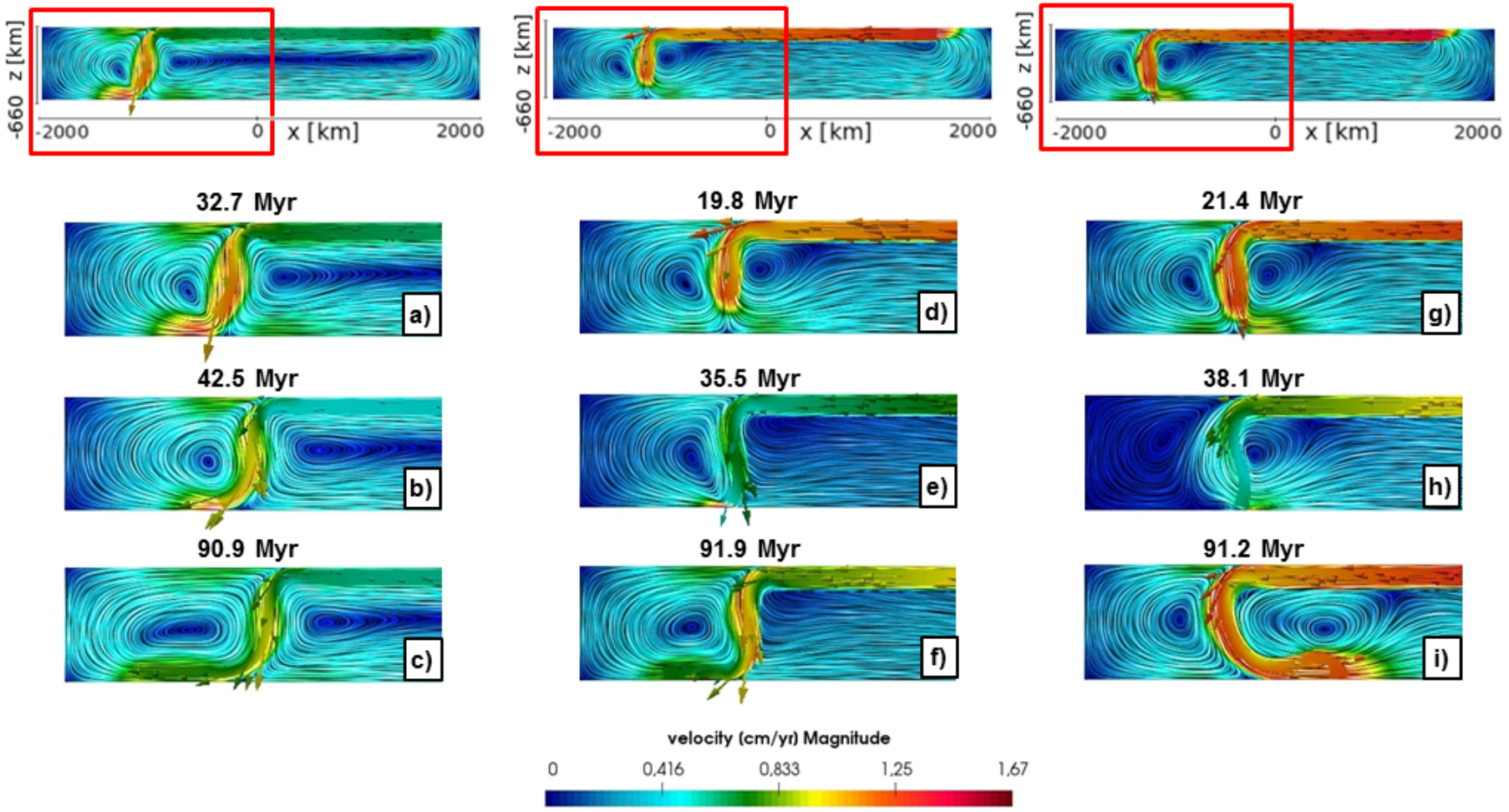

Fig. 17: Comparison of the velocity field time evolution for the RM, Sim. 1 and Sim. 2 cases with the addition of the poloidal streamlines of the velocity field.

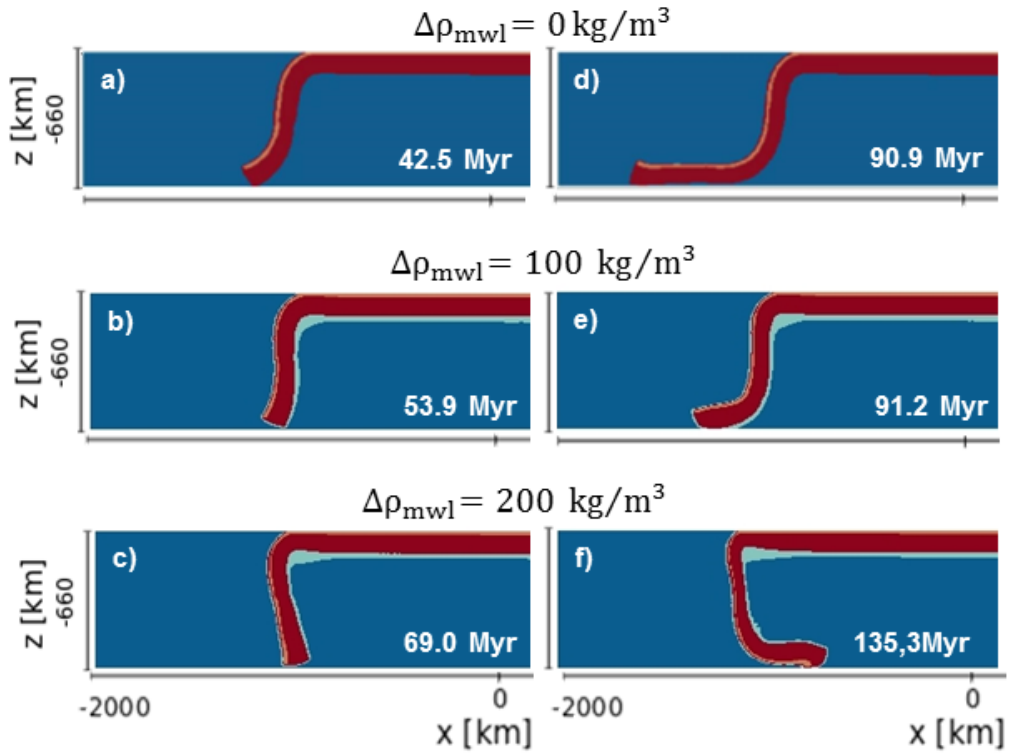

Fig. 18: Comparison showing a zoomed in section of the phase field development during the last two stages of the temporal evolution. RM with $\Delta\rho_{mwl} = 0$ [kg/m^3] a) and d); Sim. 3 with $\Delta\rho_{mwl} = 100$ [kg/m^3] b) and e); Sim. 4 with $\Delta\rho_{mwl} = 200$ [kg/m^3] c) and f).

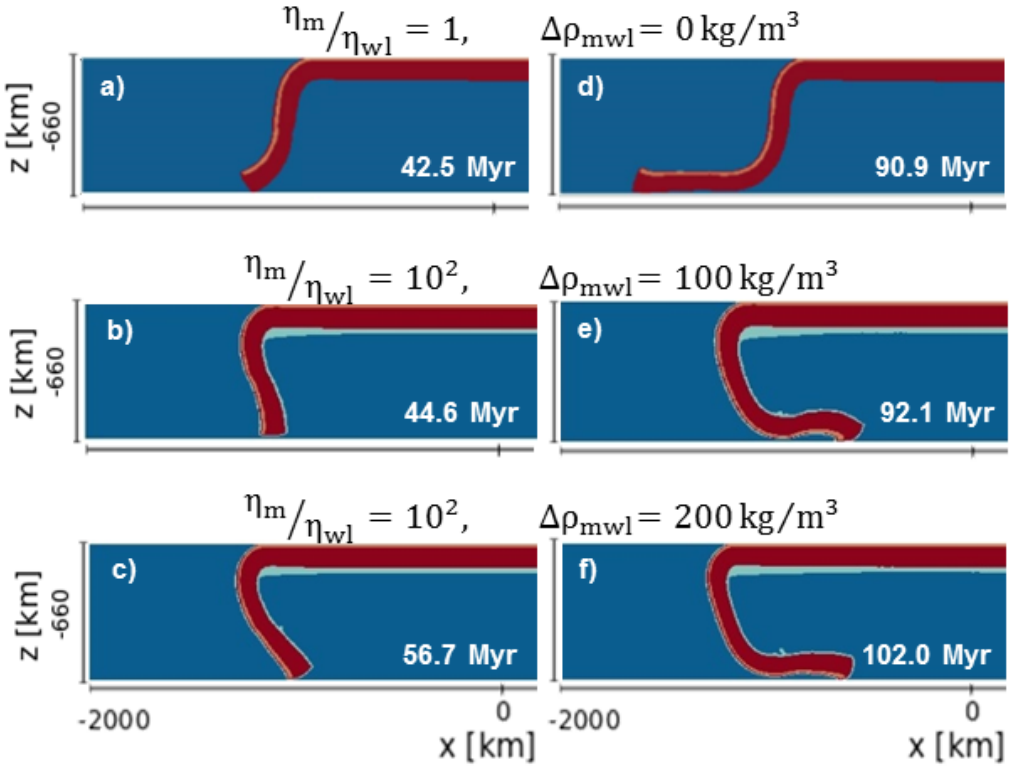

Fig. 19: Comparison showing a zoomed in section of the phase field development during the last two stages of the temporal evolution. RM with no with layer and $\Delta\rho_{mwl} = 0$ [kg/m^3] a) and d); Sim. 5 with $\eta_m/\eta_{wl}= 10^2$ and $\Delta\rho_{mwl} = 100$ [kg/m^3], b) and e); Sim. 6 with $\eta_m/\eta_{wl}= 10^2$ and $\Delta\rho_{mwl} = 200$ [kg/m^3] c) and f).

Simulation 6 has a $\eta_m/\eta_{wl} = 10^2$ and $\Delta\rho_{mwl} = 200$ [kg/m^3]. The slab touches the bottom in approx. 56.7 Myr, which an intermediate time between Sim. 3 and Sim. 4. An advancing trench is also present as for Sim. 5 but the bending of the slab is more accentuated, as shown in fig. 19 c). The final stage of the temporal evolution shows a reverse plate motion.

The presence of both a low viscosity and density channel on subduction dynamics can be observed in a comparison to the RM case in fig. 19. The resulting subduction behaviour is an advancing trench and a reversing plate, compared to the RM where the trench retreats trench and slab roll back occurs.

Further simulations (not shown in this thesis), for a greater viscosity contrast between mantle and weak layer show a general increasing in the subduction velocity without affecting the developed subduction mechanism.

3.2.4 Weak layer thickness

Simulation 7 has a h_{wl} of 10 km and a $\eta_m/\eta_{wl} = 10^2$. The subduction regime developed is approximatively the same of Sim. 1 with a slight difference in the time necessary for the slab tip to reach the bottom of the model.

Simulation 8 has a h_{wl} of 50 km and a $\eta_m/\eta_{wl} = 10^2$. For this WL thickness, the subduction regime consists of an advancing trench and a reversing plate, similarly to Sim. 2.

The effect of 10, 30 and 50 km WL thickness is shown as a comparison in fig. 20 a) d), b) d) and c) f) respectively. The weak layer thickness does not play a crucial role on subduction dynamics up to a value of 50 Km. As a value of 50 Km for the thickness of the weak layer is not realistic, the h_{wl} won't be considered as a controlling factor on subduction dynamics. These results are also in agreement with the previous simulations performed using the MVEP2 code.

The effect of the oceanic plate thickness was also tested (values ranging from 50 to 150 km) with and without a weak layer. The simulations without a weak layer are all characterised by the subduction regime valid for RM, whereas the experiments involving a weak layer resemble the subduction mechanism valid for Sim. 1, and for $h_{op} > 150$ km they develop the same trend observed for Sim. 2. An oceanic plate thickness of 150 km is anyway not realistic for the case studied.

3.2.5 The effect of a stiffer oceanic plate

Simulation 9 has exactly the same parameters as the RM except for $\eta_s/\eta_m = 10^3$. This simulation shows slab overturning and backward plate motion, fig. 21 a).

Simulation 10 This simulation is exactly the same as Sim. 9 expect for the presence of a weak layer at the LAB. The simulation shows slab overturning and backward plate motion, see fig. 21 c).

From fig. 21, it can be seen that the effect of a stiffer oceanic plate is to develop a reverse plate motion (fig. 21 a) c)), for both the cases with and without a weak layer. However Sim. 10, which involves a weak layer, develops a faster subduction mechanism. This case was tested to further prove the reliability of the model using previous works, as this is a

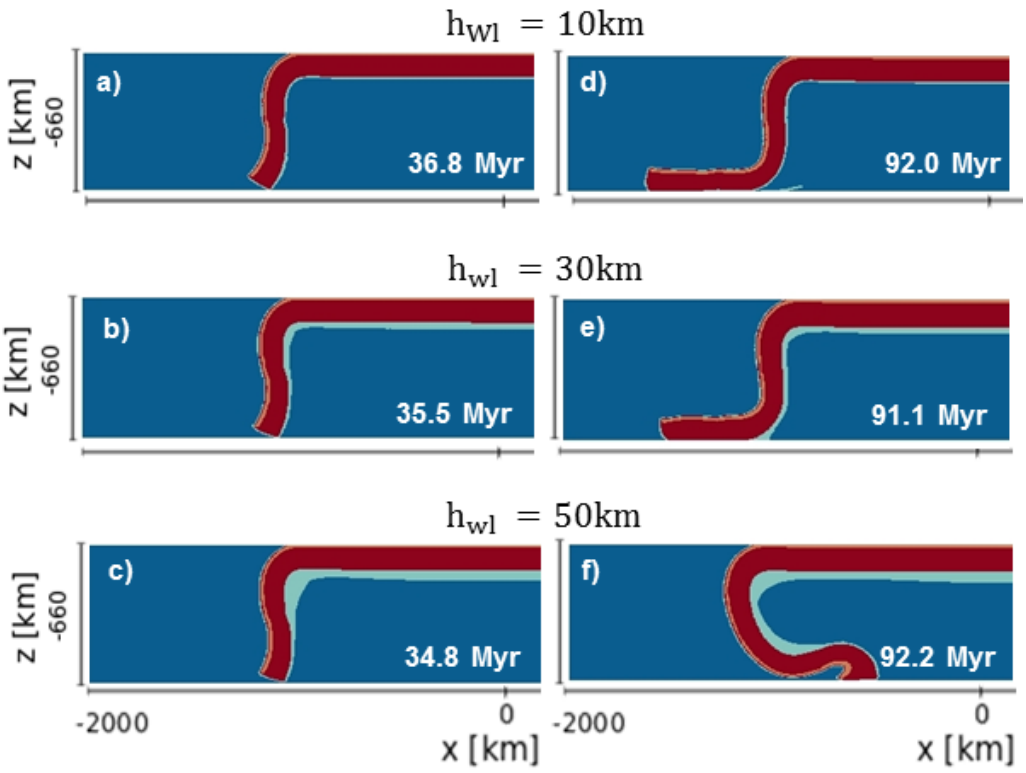

Fig. 20: Comparison showing a zoomed in section of the phase field development during the last two stages of the temporal evolution. Sim. 7 with h_{wl} of 10 km and $\eta_m/\eta_{wl} = 10^2$ a) and d); Sim. 1 with h_{wl} of 30 km and $\eta_m/\eta_{wl} = 10^2$ b) and e); Sim. 8 with h_{wl} of 50 km and $\eta_m/\eta_{wl} = 10^2$ c) and f).

primary order effect for a stiffer oceanic subducting plate well known from the literature, see also 4.

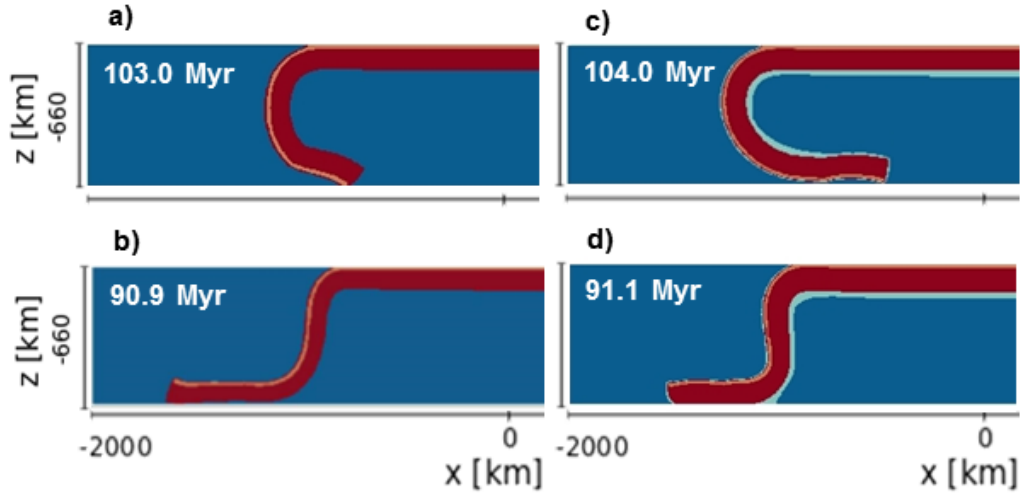

Fig. 21: Comparison showing a zoomed in section of the phase field development during the last stage of the temporal evolution. Sim. 9 with $\eta_s/\eta_m = 10^3$ and $\eta_m/\eta_{wl} = 10^0$ c); RM with $\eta_s/\eta_m = 10^2$ and $\eta_m/\eta_{wl} = 10^0$ b); Sim. 10 with $\eta_s/\eta_m = 10^3$ and $\eta_m/\eta_{wl} = 10^2$ c); Sim. 2 with $\eta_s/\eta_m = 10^2$ and $\eta_m/\eta_{wl} = 10^2$ d).

3.2.6 The effect of a different trench decoupling mechanisms

The effect of different trench decoupling mechanisms was explored as the weakening of the lithosphere in the models is necessary to detach the slab from the surface and to allow the plate to move freely.

Several tricks are used to allow subduction to take place in simulations, for example the use of "Drucker Pager yield criterium" type plasticity to locally yield the strong slab, as for previous models (see also fig. 8) or the addition of a soft buoyant layer (sticky air), as it shown in fig. 22. In this thesis work the Drucker-Prager yield criterion was applied to the models shown in the thesis, for a friction angle and cohesion value of 30° and 20 MPa respectively. In this section, the effect of a true free surface are explored in a comparison to the simulations involving a weak plastic upper layer. These two methods are presented, as they converge to the same solution, possible due to the high resolution provided in the models. The simulations performed using a free surface boundary condition employ a newtonian rheology whereas, the simulations use free slip as top boundary condition have a visco-plastic rheology.

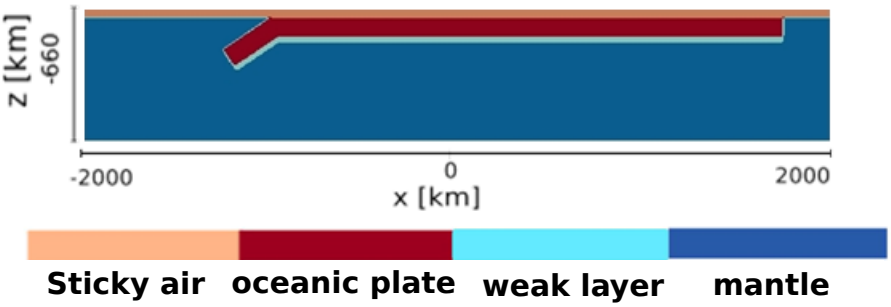

Fig. 22: A 40 km thick "sticky air" layer ($\rho_{\text{air}} = 1[kg/m^3]$ and $\eta = 10^{18}[Pa \cdot s]$) was used in order to mimic the effect of a free surface. The subducting plate is 100 km thick, 2000 km wide and 2750 km in length. The model employs a WL of 30 km thick, and the oceanic plate has a viscosity contrast in the respect to the mantle of 2 orders of magnitude. The top boundary of the box has a free surface boundary condition and all the others modelling box boundaries have a free slip condition.

Simulation 11 and **Simulation 12** are the correspondent of the RM and Sim.1. The model comparison is shown in fig. 22, from which can be observed that the overall subduction regime remains the same with only a slight difference in the time necessary for the slab tip to reach the bottom of the model for the simulations involving a free surface top boundary condition, see fig. 23 a) e) in comparison to and c) d). Thus, the models show the predominance of the viscous behaviour over plasticity. Moreover, the presence of a weak layer does affect subduction dynamics independently from the decoupling mechanism chosen for the models.

Models that employ a free surface stabilization algorithm as a top boundary condition were also obtained using MVEP2, and are shown in section 5.

3.3 3-D simulations

3.3.1 3-D weak layer viscosity

3-D reference model The reference model chosen for the 3-D investigation was built from the 2-D reference model and adapted for solving a 3-D case.

The 3-D RM time evolution shows both trench retreating and slab roll back mechanisms. The time evolution is similar to the RM in 2D, however the presence of a third dimension generates variations in the development of the velocity field.

0-20 Myr The first time stage sees the dynamic initiation of subduction,

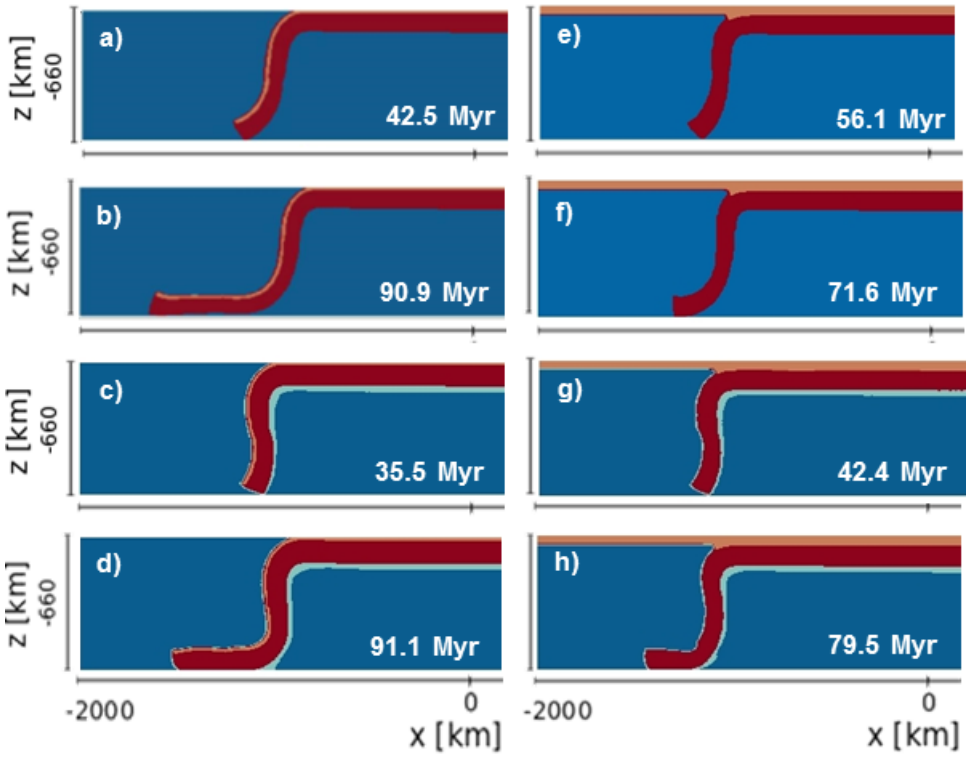

Fig. 23: Comparison showing a zoomed in section of the phase field development during the last two stages of the temporal evolution. RM and Sim.1 involve a weak plastic upper layer of 10 km thick a) & b) and c) & d). Sim. 11 and Sim. 12 involve a sticky air layer at the top of the model of 40 Km thick e) & f) and g) & h).

similarly to the to the 2D case. The trench retreats and the slab increases its dip angle reaching a value of approx. 70°, see fig 24, a). At this stage is also possible to appreciate the development of the toroidal component of the velocity field responsible for the lateral narrowing of the plate free margin, fig. 27, a).

20-40 Myr The second phase is characterised by an abrupt decrease in v_{total}, with a minimum at 40 Myr when the slab reaches the bottom of the model. At this stage, all the velocity components have decreased expect for the y velocity component, which acts to deform the slab free tip and v_{plate} is ≈ 0, see fig. 24, b).

40-92 Myr In this final stage, a new subduction configuration is reached. The retreating trench rate increases, v_{total} increases again and the slab dip angle reaches a value of about 80-90° while its tip lies parallel to and on the top of the mid mantle discontinuity, see fig. 24, c). The toroidal component of the velocity field acts deforming the free plate edges, see fig. 27, b).

In 92 Myr, the trench retreats 350 km. The rear edge of the oceanic plate is displaced 700 km starting from its original starting position. The plate average horizontal velocity is 0.760 cm/yr, despite the slab roll back active mechanism (fig. 26, a)). The plate width decrease of 320 km in 92 Myr, undergoing a narrowing of the 16 %, (fig. 26, b)). The strongest component of the velocity field over the entire time evolution is v_{slab} approx. 1.0 cm/yr. The second higher velocity developed is v_{plate}, which is high during the first and the third stages and reaches a minimum value of 0 cm/yr during the second phase of the subduction evolution. The $v_{lateral}$ component of the velocity field is higher during the last stage of subduction and acts mainly by deforming the plate free edges.

Simulation 12 is the 3-D correspondent of the 2-D Sim. 1. This model has a distinct behaviour as characterised by a quasi stationary trench and reverse plate motion.

0-20 Myr The first stage of subduction, starts by the progressively increasing in v_{total} until ca. 20 Myr. At this stage v_{slab}, v_{plate} and $v_{lateral}$ reach a peak value of approx 1.3 cm/s, 1.1 cm/s and 0.7 cm/s respectively, see fig. 25, a). As for the previous case, at this stage is possible to appreciate the development of the toroidal component of the velocity field mainly responsible for the lateral narrowing of the plate free margin, fig. 27, c).

20-40 Myr As for the other subduction models, during the second stage of the temporal evolution, the velocity drastically drop. The slab tip reaches the bottom of the model at ca. 35 Myrs (5 Myrs earlier than for the 3-D RM, and approximatively the same time of its correspondent 2-D simulation). During this stage, the trench retreats slightly and plate velocity decreases, see fig. 25, b). However, the lateral component of the velocity field begins to deform the slab free tip of the slab. The slab assumes an average dip angle of about 90°.

40-92 Myr The slab interaction with the bottom of the model bounding box results in a reclined U-shape for the slab. The WL also uplifts at the rear edge of the plate. Only when the slab tip overcomes the bending resistance generated at the bottom of the model, the velocity of the slab can increase again. During this phase the slab tip also folds and deforms, see fig. 25, c). The trench advances, almost reaching its original position, see fig. 26, c). However the fixed edge of the hinge is slightly displaced backwards while the free edge of the hinge is a bit advanced, see fig. 26, d). At this

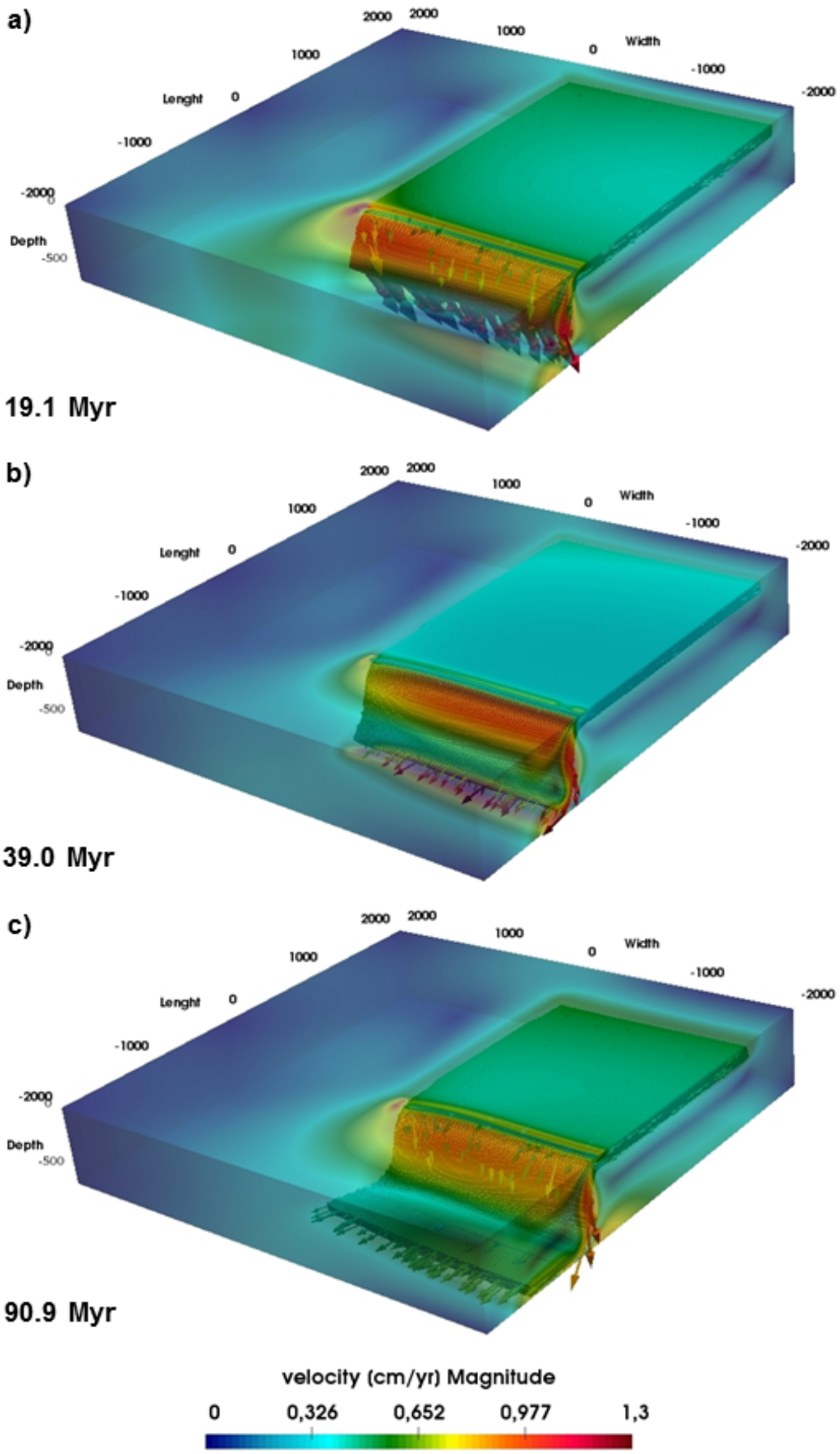

Fig. 24: The velocity field long term evolution for the 3-D RM (with no WL) is represented by a), b), c). A final steady state configuration was reached in 90.9 Myr.

stage the horizontal plate velocity becomes the strongest component of the total subduction velocity field. The toroidal component of the velocity field is still active and deforms the free plate edges, see fig. 27, d).

The rear edge of the oceanic plate is displaced 900 km starting from its original starting position, see fig. 26, c). The plate average horizontal velocity is 1.0 cm/yr, despite a quasi stationary trench active mechanism. The plate width decreases 400 km in 92 myr, undergoing a narrowing of 20 %, see fig. 26, d).

In summary, the 3-D RM is defined by trench retreat and slab roll back mechanisms, where v_{slab} is the highest component of the velocity field over the entire time evolution and the plate undergoes a narrowing of the 16 % in 92 myrs. Sim. 12 shows a compressively higher v_{slab}, a quasi stationary trench and a reverse plate motion, the highest velocity, v_{plate}, is developed at the latest stage of the time evolution, with a narrowing of the plate of the 20%.

Deformation flow time evolution The 3-D velocity field can be subdivided in terms of poloidal and toroidal velocity components, as it shown in fig. 37. The toroidal flow component is developed on the plane perpendicular to the z axis and the poloidal flow component can be observed on the plane normal to the x axis. Both the components are active since the earliest subduction stage, fig. 27, a) and c).

Similar to both the models is the development of two convective cells part of the toroidal deformation flow (e.g. fig. 27, a) and c)), that move from the right side to the left side of the model at the transition between the first stage and second stage of the time evolution and move backward during the transition between the second and third stage of the temporal evolution of the models.

Different for the two models is the development of the poloidal deformation flow. Sim. 12 also shows a strong flow component behind the dipping part of the slab.

A similar correlation between the development of a particular subduction mechanism, velocity field and deformation flow was also observed for the 2-D simulatuions, fig.17.

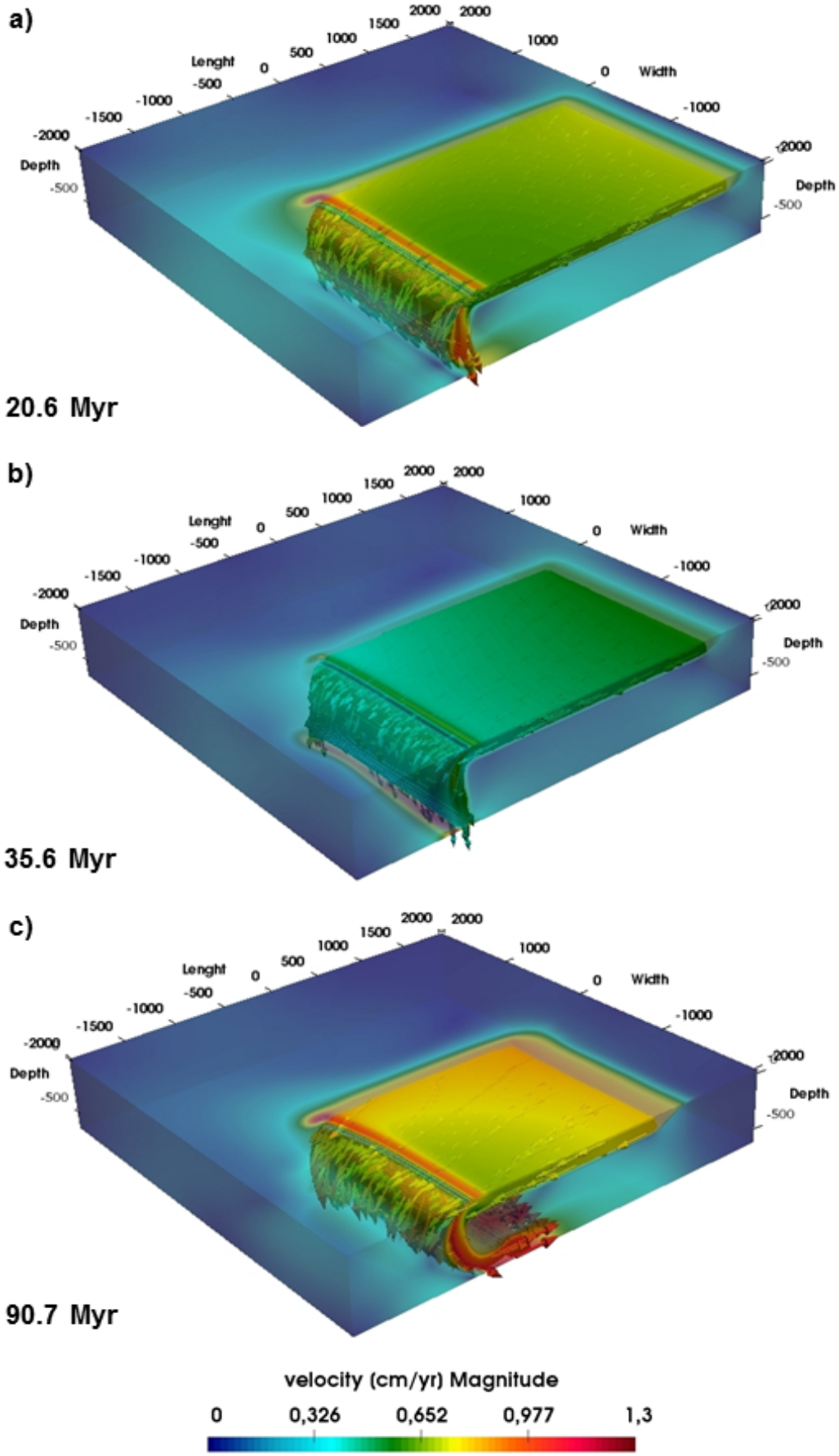

Fig. 25: The velocity field long term evolution for the 3-D Sim. 13 (with WL) is represented by a), b), c). A final steady state configuration was reached in 90.7 Myr.

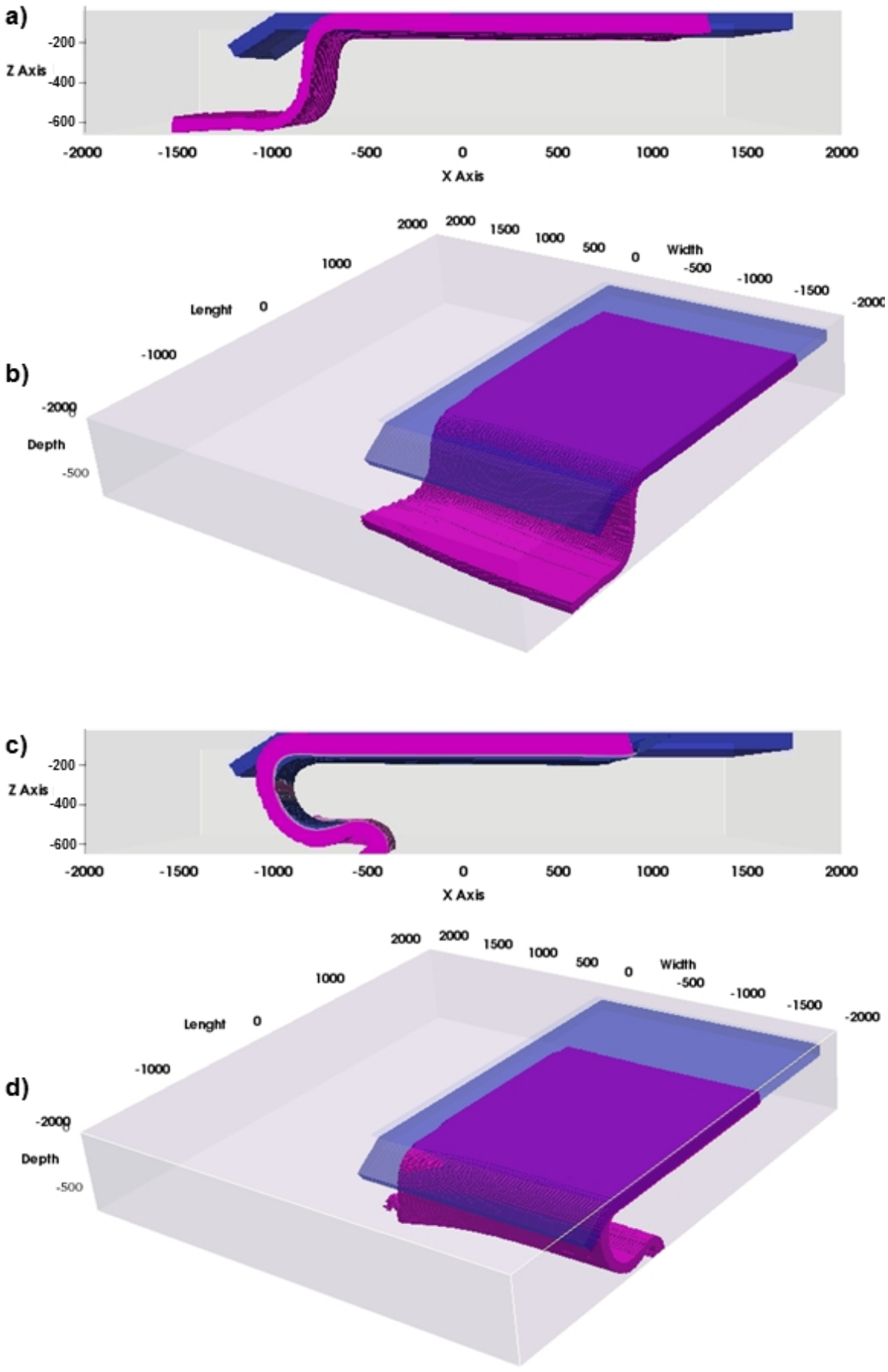

Fig. 26: A comparison of the initial and the final phase field deformation stages. Violet and magenta are the initial and the final stages respectively. a) and b) refer to the 3-D RM and c) and d) refer to the Sim. 13 model.

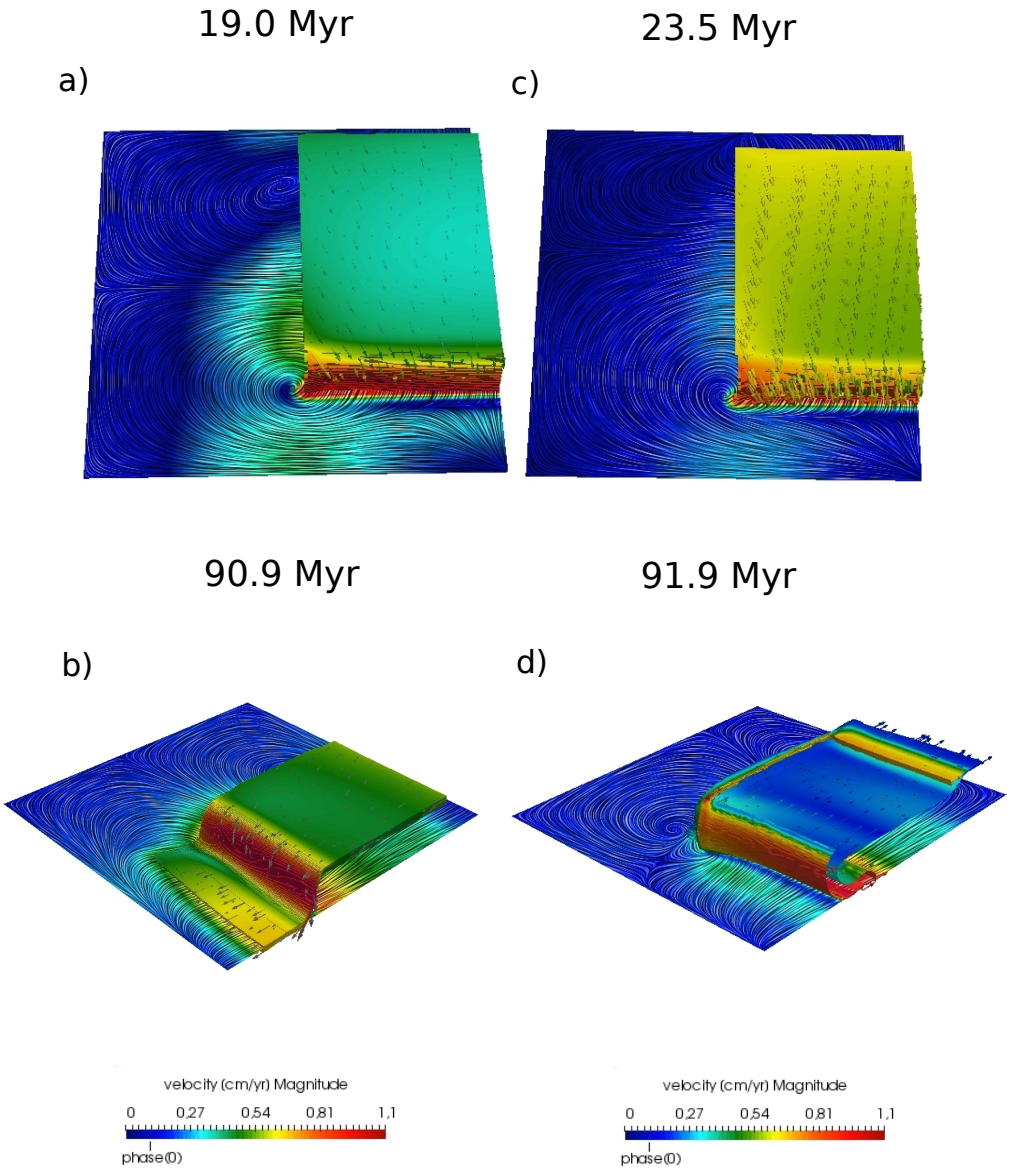

Fig. 27: A comparison of the initial and the final time deformation stages showing the development of the toroidal component of the velocity field. a) and b) refer to the 3-D RM and c) and d) refer to the Sim. 13 model.

4 Discussion

4.1 The effects of a weak layer at the LAB boundary on subduction dynamics

The presence of a weak layer at the LAB boundary can primarily generate a variety of subduction regimes. The different subduction regimes obtained during this thesis work are shown in fig. 28. These subduction regimes are characterised by a distinctive slab shapes, velocities and relative deformation flows, and are a function of the different variables tested during this thesis work, such as viscosity and density of the weak layer.

Four distinct types of subduction mechanisms were identified and classified based on the final stage of the long-term subduction evolution. Each subduction type has also an associated trench and plate motion with resultant slab morphology:

1. Type I: either 2-D or 3-D continuously retreating trench accompanied by predominantly slab roll back and a forward plate motion, resulting in a flat-lying slab, fig. 28 a).
2. Type II: a 2-D generally quasi stationary trench associated with a forward plate motion, resulting in a flat-lying slab, fig. 28 b).
3. Type III: a 2-D continuously advancing trench accompanied by predominant backwards plate motion that results in an overturned, flat-lying slab with a little recumbent fold, fig. 28 c).
4. Type IV: a 3-D generally quasi stationary trench associated by predominant backwards plate motion that results in an overturned, flat-lying slab with a little recumbent fold, fig. 28 d).

The type I subduction regime develops for the case of an oceanic plate subducting into the mantle with no weak layer. The type II develops for viscosity and density contrast values between mantle and weak layer which are intermediate between those for type I and type III subduction. Type III develops for a relatively high value of viscosity and density contrast between the mantle and the weak layer. Type IV develops in an equivalent 3-D case of the type II of subduction.

This variety of subduction mechanisms correlate with the predominance of one component of the velocity field over the other/s. Thus, calling V_{slab} the slab sinking velocity, V_{plate} the horizontal plate velocity and $V_{lateral}$ the lateral velocity, it was observed that:

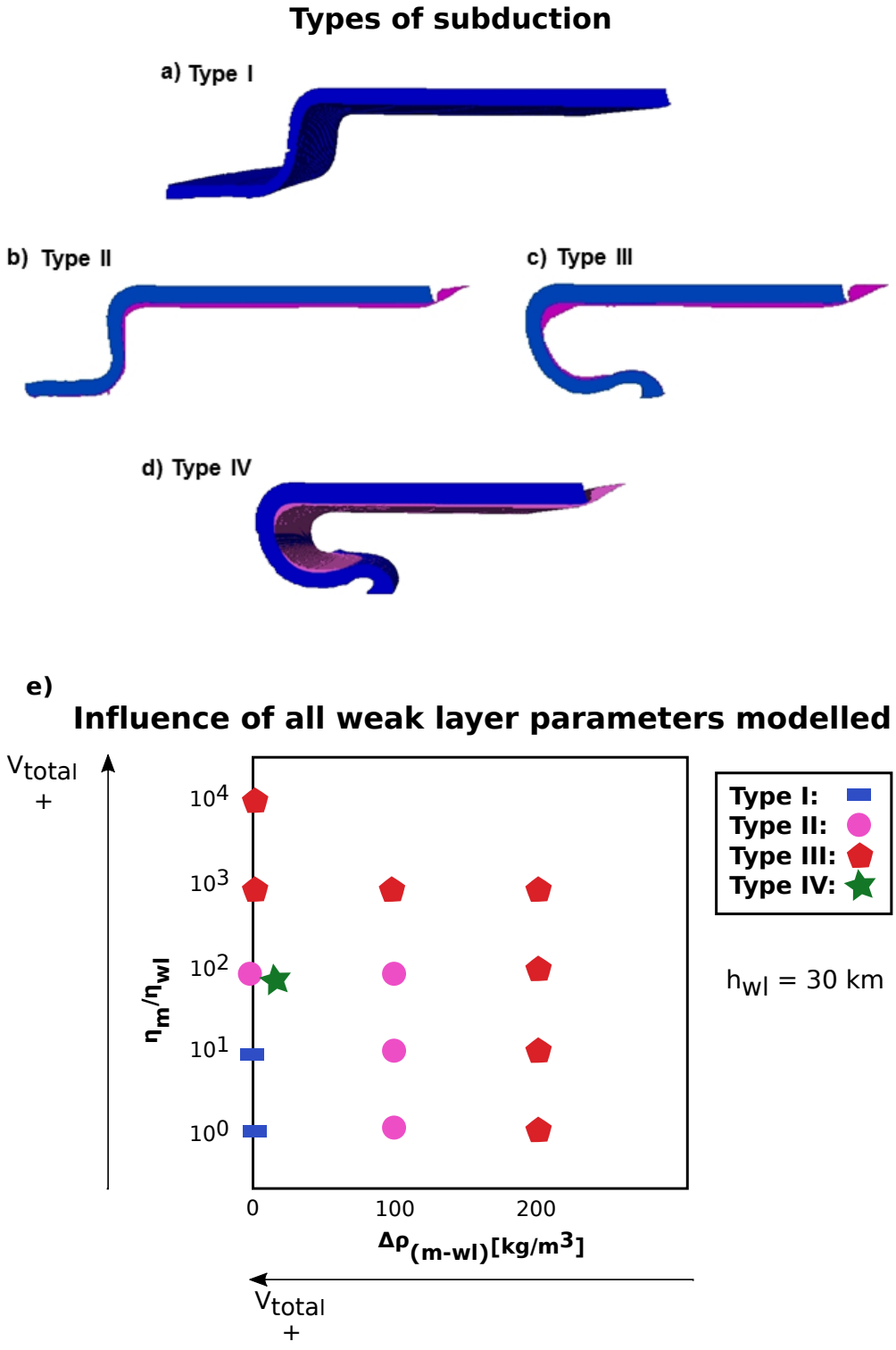

Fig. 28: Figure illustrating the distinctive subduction regimes developed during this thesis work type i, type II, type III and type IV in a), b), c) and d), respectively. The different subduction types develops as a function of viscosity and density contrast between mantle and weak layer parameters tested represent in e).

– Type I always develops the strongest slab sinking velocity component over the other two: $|V_{slab}| > |V_{plate}| > |V_{lateral}|$.

– Type II develops the highest plate velocity component in stages 1 and 2, but during the final subduction stage the two components become nearly the same: $|V_{slab}| \approx |V_{plate}|$.

– Type III always develops the highest plate velocity component: $|V_{slab}| < |V_{plate}|$.

– Type IV develops the highest sinking velocity during stages 1-2, but during the final subduction stage, the plate velocity becomes the highest component of the velocity field: $|V_{lateral}| < |V_{slab}| < V_{plate}|$.

Therefore, the motion of the trench showed a correlation with the predominance of either $|V_{slab}|$ on $|V_{plate}|$ or vice versa, as follow :

- $|V_{slab}| > |V_{plate}|$ trench retreats,
- $|V_{slab}| < |V_{plate}|$ trench advances,
- trench is quasi stationary when there is no strong predominance of one component over the other, over the entire model time evolution.

It was also observed a correlation between the direction of the plate motion and the predominance of either $|V_{slab}|$ or $|V_{plate}|$ at the finale stage of subduction:

- $|V_{slab}| > |V_{plate}|$ plate moves forward,
- $|V_{slab}| < |V_{plate}|$ plate overturns and moves backwards.

4.1.1 Place forces

Fig. 29, shows the principle forces thought to affect the movements of the lithospheric plates in the simplified scenario modelled in this thesis. This drawing is edited after Rogers and Blake (2008). Assuming a static equilibrium, the net force balance that needs to be respected is the following:

$$F_{SP} + F_{RP} = R_S + R_B + R_R + R_{TF}. \tag{29}$$

The forces on the left side promote motion and are respectively, F_{SP} the slab pull force and F_{RP} the ridge push force. The forces on the right side impede movement and are respectively, R_S the slab resistance force, R_R the

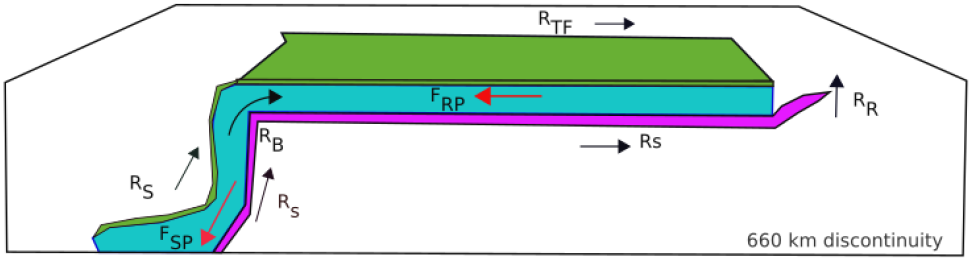

Fig. 29: Figure illustrating the influence of plate forces on the problem investigated, edited after Rogers and Blake (2008).

ridge resistance force, R_B the bending resistance force and R_{TF} the transform fault resistance force. Other forces have been neglected such as the continental drag force, the overriding plate resistance force, the collisional resistance force and the ridge suction force as an overriding plate, topography and temperature evolution were not modelled here. The different components have been previously explained in section 1.1.1.2.

For the sake of simplicity, the slab pull is assumed to be the main driving forces of subduction, plate deformation and mantle flow. With this assumption F_{SP} is balanced by R_S, as follows:

$$F_{SP} = R_S. \tag{30}$$

The slab pull force can be approximated as:

$$F_{SP} = g\Delta\rho_{sm}V \tag{31}$$

where g is the gravity acceleration, $\Delta\rho_{sm}$ is the density contrast between the slab and mantle, and V is the volume of subducting slab. The slab resistance force can be approximated as:

$$R_S = \frac{\Delta v}{h_{wl}}\eta \tag{32}$$

where Δv is the velocity contrast across the weak layer, h_{wl} and η are the thickness and the viscosity of the weak layer, respectively.

4.1.2 The influence of the different weak layer parameters modelled

The different subduction regimes obtained here, are a function of the different WL rheological and geometrical parameters modelled: viscosity, density and thickness, see also fig. 28 e). It was observed that the total subducting velocity V_{total} increases with (i) increasing viscosity ratio between mantle and weak layer η_m/η_{wl}, (ii) decreasing density contrast between mantle and weak layer $\Delta\rho_{mwl}$, and (iii) increasing weak layer thickness h_{wl}, as:

$$V_{total} \propto \frac{\eta_m}{\eta_{wl}} \frac{1}{\Delta\rho_{mwl}} h_{wl} \tag{33}$$

A first order viscosity dependence can be explained using equation 32. Indeed keeping the mantle viscosity constant and reducing the layer viscosity, the velocity contrast has to increase to keep the net force balance.

The same is valid for the thickness. If the thickness increases velocity needs to become bigger in order to respect the force equilibrium. However, It was observed that the thickness plays not a main rule in defining the main subduction regimes.

Density contrast between the mantle and the weak layer has a diminishing effect on the magnitude of the slab pull force. Hence, negatively affecting the magnitude of the slab velocity.

4.2 Comparison with similar work on subduction zone

All the models presented in this thesis share in common the same three subduction temporal evolution stages as found in literature, see for example Stegman et al. (2010) and Bellahsen et al. (2005). These evolution stages are: 1) sinking of the slab through the upper mantle, (2) transient slab/lower boundary interaction (3) a new stationary configuration when the slab lies at the bottom of the model, as described and shown in section 3.

To further prove the reliability of the models using previous works, a primary order effect, namely the increase in viscosity contrast between the slab and the mantle of one order of magnitude resulting in the overturning of the slab, was tested and shown in section 3.2.5. The morphological temporal evolution of the simulations was consistent with those obtained in numerical and laboratory experiments of Stegman et al. (2006, 2010), and Funiciello et al. (2008); Bellahsen et al. (2005); Schellart (2004), respectively (e.g. see fig. 30). Moreover, the same primary order effect was obtained for the case

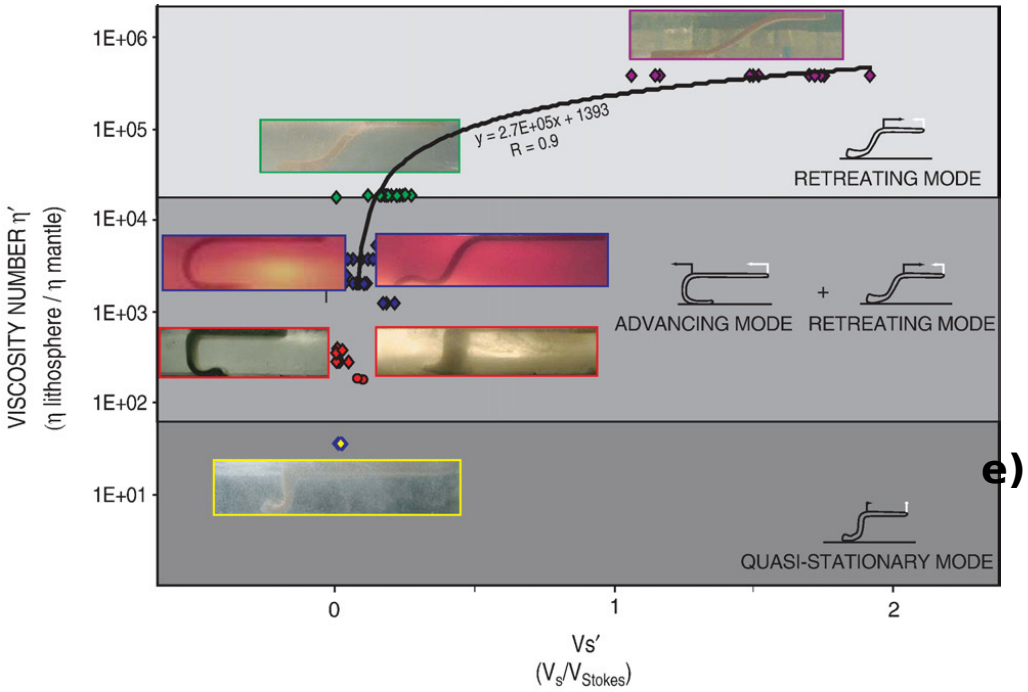

Fig. 30: Figure from Funiciello et al. (2008) showing the different behaviour of free ridge laboratory experiments for a different slab/mantle viscosity number and normalised subduction velocity.

of a WL at the base of a stiffer tectonic plate resulting in a faster subduction dynamic, previously shown in fig. 21.

The simulations performed in this thesis are simplified in terms of rheology, however they obtain some similar features seen when also more complex rheology is modelled, see for example Stegman et al. (2010). These features were obtained considering only the presence of a weak layer at the LAB boundary which was not included in previous 2-D and 3-D models, see fig. 31. Fig. 31 shows a comparison between the regimes presented here and the work of Stegman et al. (2010). Some of the additional differences developed in the features (i.e. buckling of the slab at the bottom of the model) can be due to the fact that lower mantle layer is not modelled here.

The numerical results obtained for the 3-D simulations are morphologically comparable with the 3-D laboratory experiments for a purely viscous plate material from Schellart (2004), including induced flow occurring around the lateral free edge of the slab and the forced convex shapes of the hinge in the direction of retreating, as shown in fig. 32 and fig. 33. Thus, the models have in common the active deformation of the hinge operated by the toroidal component of the flow, see fig. 32, a) and b) and fig. 33 b).

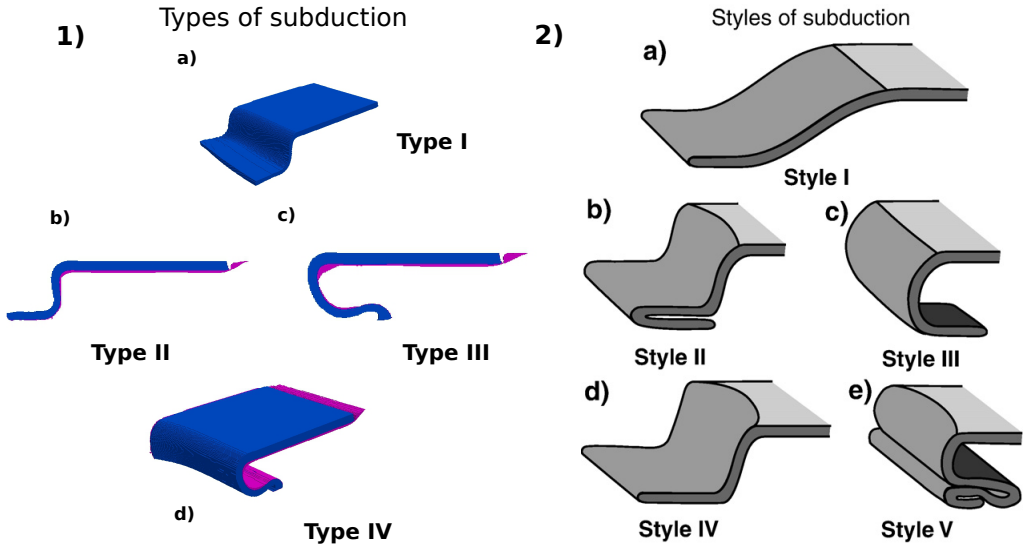

Fig. 31: A comparison between the types of subduction developed during this thesis work, and the styles if subduction developed by Stegman et al. (2010) shown in a) and b) respectively.

Schellart and Stegman et al., also report that the toroidal component of flow is established during the earliest stage of subduction, which is in accordance with the results shown previously in fig. 27 a), c). For the 3-D models, the toroidal flow changes enough to influence the dynamics developed in 3-D compared to those in 2-D (see fig. 34). This is mainly associated with the lateral deformation of the plate and the slab free tip (see fig. 32). For the RM case, it was observed that the retreating rate increases from approx. 2.7 mm/yr to 3.8 mm/yr when modelling from 2-D to 3-D, see fig. 34 a) and b). Whereas for Sim. 1 the effect of a third dimension can directly affect the subduction regime developed, changing from type II to type IV, see fig. 34 c) and d). In this case the toroidal flow component participate actively to the deformation mechanism. The results obtained demonstrate that both the toroidal and poloidal circulations can significantly affect the subduction mechanisms, which is in agreement with Kincaid and Griffiths (2003) and Funiciello et al. (2003).

According to Funiciello et al., mantle flow in subduction zones cannot be correctly described by models assuming a two-dimensional steady state process. The intermittent toroidal and poloidal components of mantle circulation can play a crucial role in modifying the subduction regime and the trench geometry and evolution, as shown in fig. 34.

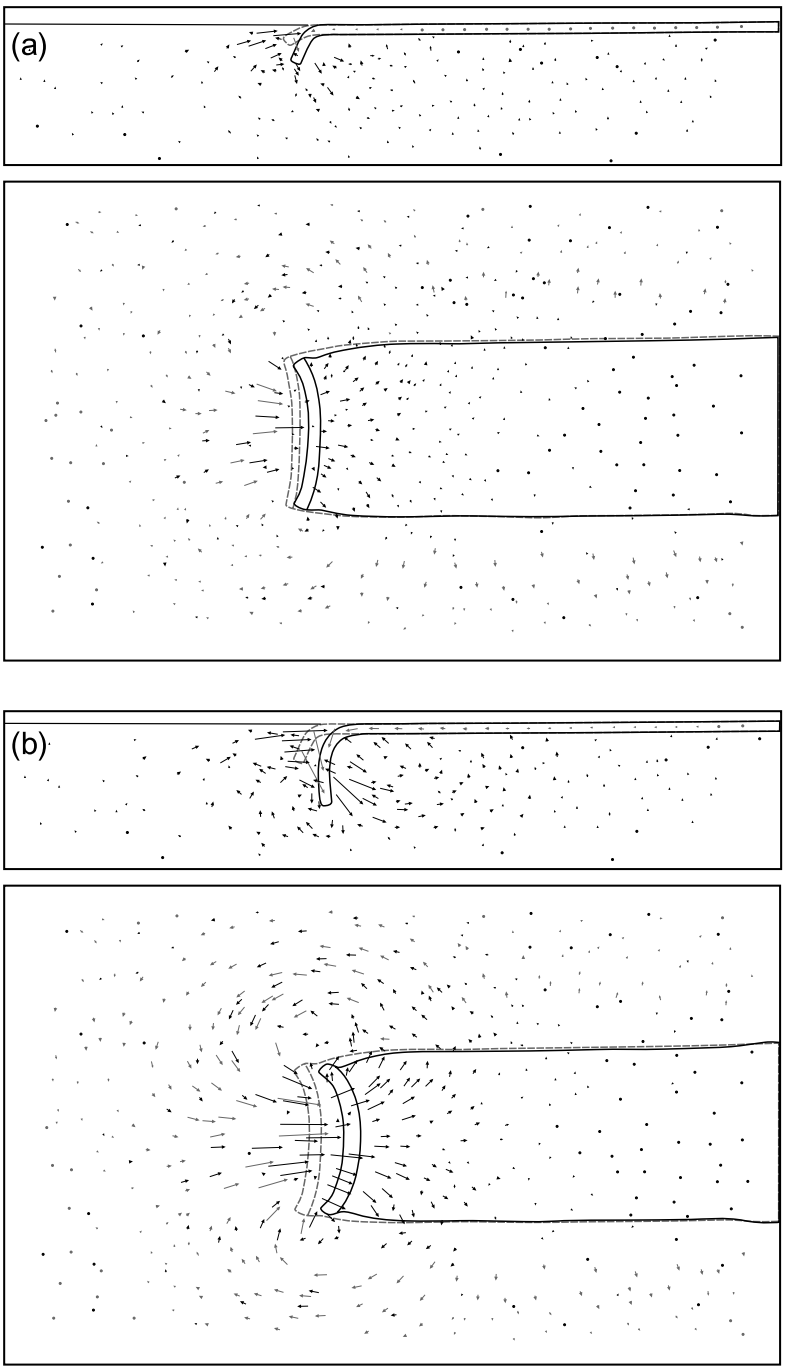

Fig. 32: Line drawings of side-view and bottom view perspective, illustrating subduction-induced flow pattern in glucose syrp during the first two stages of subduction a) and b) respectively, from Schellart (2004).

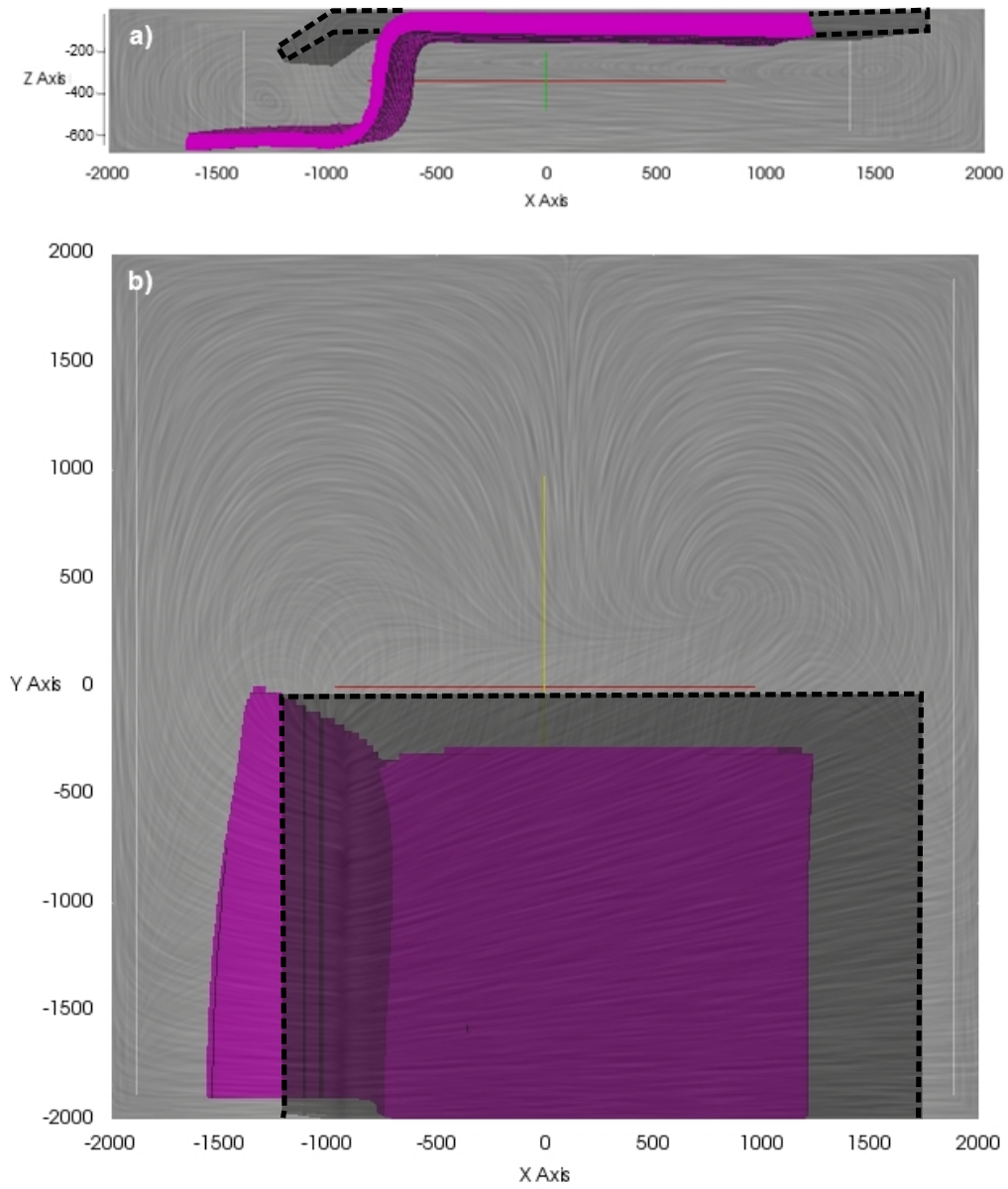

Fig. 33: Stream line of side-view and bottom view perspective a) and b) respectively for the RM case. a) and b) also illustrate subduction-induced flow pattern and a comparison between the first (dashed black line) and the final stage (magenta slab) subdution time evolution stages.

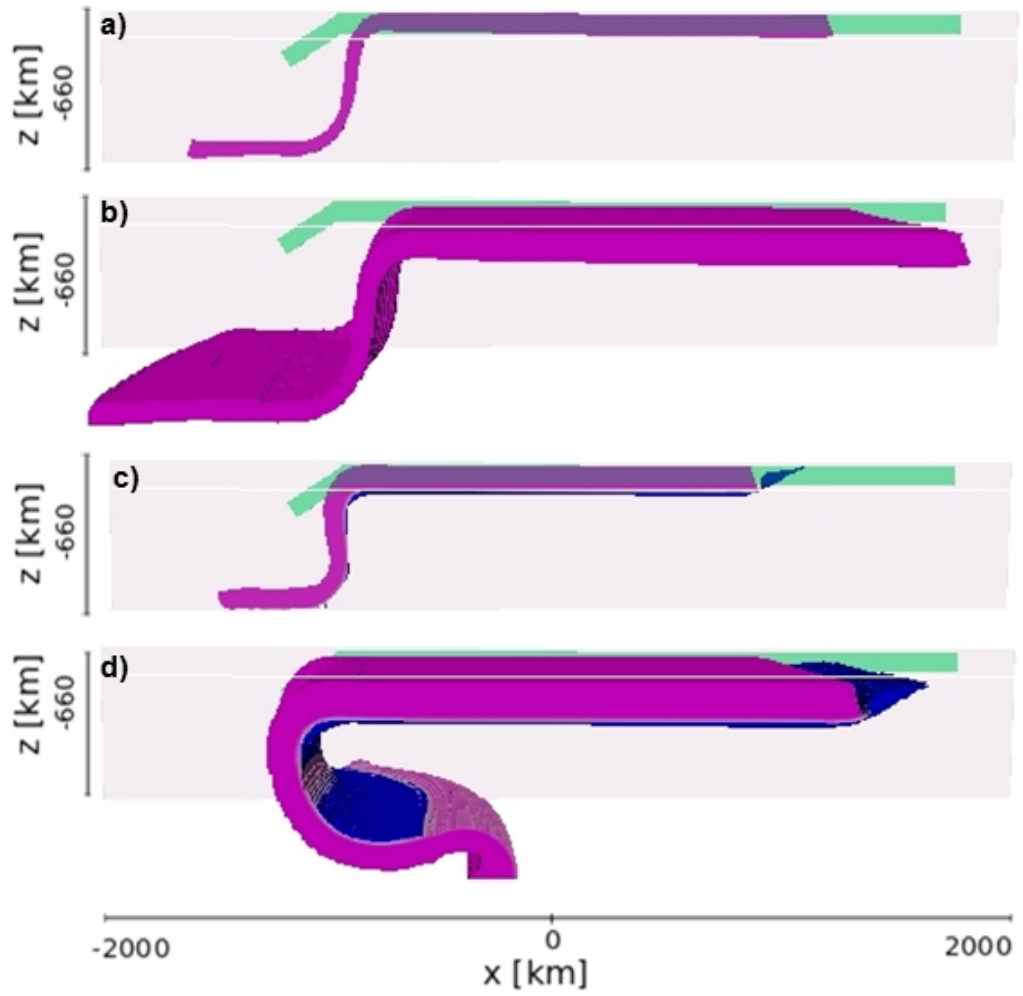

Fig. 34: Comparison of the phase field time evolution developed in 2-D and 3-D. a) and b) refer respectively to the 2-D and 3-D cases for the RM. c) and d) refer respectively to the 2-D and 3-D cases for Sim. 1 and Sim. 13.

4.3 Model limitations and new purposes

As models are simplifications of reality, each modelled phenomena has is own limitations. Amongst the effects neglected in the thesis are, in perceived order of increasing importance, temperature dependent visco-elasto-plastic rheology, overriding plate, vertical viscosity contrasts in the mantle (due to the missing of the lower mantle layer), sphericity, temperature diffusion, phase transition effects other than increase in viscosity, power-law rheology and other geometrical effects.

In the simulations all these factors were not considered, although they can play an important role on the Earth's dynamic mechanisms and evolution. Therefore, the simulation results are indicative of the first order behaviour of the system involving the presence of a weak layer. For example, the correlation between the development of the different subduction mechanisms as a function of the different weak layer parameters modelled: viscosity, density. More over, no previous geodynamics models on this topic exist and in order to gain a better understanding of the first-order physical principles and effects, this Master thesis intentionally applies to solving a simple model. Simple models have been shown to reproduce results of much more complicated patterns while employing relatively simpler physics.

Future investigations which concentrate on the role of temperature dependent visco-elasto-plastic rheology affecting the behaviour of the system will be able to better address how the subduction regimes and velocities evolve through time as the oceanic plate moves into progressively thinner (younger) or thicker (older) lithosphere. However, the role of elasticity in controlling slab related deformation is still controversial. The results obtained by a large number of authors discussed in Becker and Faccenna, indicate that elasticity may not significantly effect subduction dynamics, see also Kaus and Podladchikov; Kaus and Becker; Schmeling et al..

The complessive advancing nature of the models could also be due to the lack in the physical presence of an overriding plate. According to Yamato et al. the role of the overriding plate is an important factor because a subduction zone without an overriding plate is not realistic. Thus, testing the role of a WL at the LAB on subduction zone which involve the presence of an overriding plate will be a prospective for future work. However, the trench velocities in our models should not be too much over estimated as we have neglected the temperature evolution.

Additionally, mantle heterogeneities such as mid mantle discontinuity

have been shown to play a significant influence in defining the shapes of subducting slabs at the boundary. Thus, considering the role of the lower mantle layer in the future simulations will be very interesting for exploring the morphological evolution of the modelled subduction zones.

4.4 Applications to natural subduction zones

Modelled results are difficult to extrapolate to natural systems. This is because of the lack of a realist scenario, proper scaling for temperature dependent viscosity and because trench kinematics can be influenced by the topography, and also by the presence of the lower mantle.

However, the results obtained well suit to the localisation of the strain rate and accommodation of the stress drop at the LAB as predicted by Stern et al. (2015), and shown in fig. 35 b) and c). Stern et al. used a seismic reflection technique to image the base of the tectonic Pacific plate subducting underneath the Australian plate. The author also predicted all the relative motion between the Pacific plate and underlying asthenospheric mantle, as accommodated in a zone of 10 km thick producing a strain rate of 3×10^{-13} s^{-1}. In the case modelled here the strain rate and shear stresses are approximatively 8.5×10^{-15} s^{-1} and 2.1×10^{5} MPa, respectively. The channel has a viscosity of 2.5×10^{19} (Pa·s), thickness of 30 km and a dynamically induced within the weak layer, Δv, of 0.8 cm/yr (9 times slower than the one of the hotspot reference frame used by Stern et al. (2015). Fig. 35 shows a comparable trend to the one reported from Stern et al. (2015).

The pacific trench is advancing. Natural subduction zones advance and retreat. The models studied in this thesis show evidence of advancing and retreating trenches. Faccenna et al., using a recent compilation of a global data set found that the motion of trenches (either advancing or retreating with respect to upper plates) scales with their corresponding subducting plates motion, see fig. 36. Based on experimental tests, they found that subduction of strong slabs inside the upper mantle correctly predicts these kinematic relationships. In the modelled results, it was possible to observe a similar relationship where the highest plate velocities are expected for the advancing trenches and the lower plate velocities are expected for the retreating trenches. The trench retreated 250 km and 350 km in the type I experiments, for the 2-D and 3-D cases respectively. The trench advanced 100 km for type III experiment. Absolute hinge-retreat rates in nature are difficult to determine, because they have to be determined in some sort of

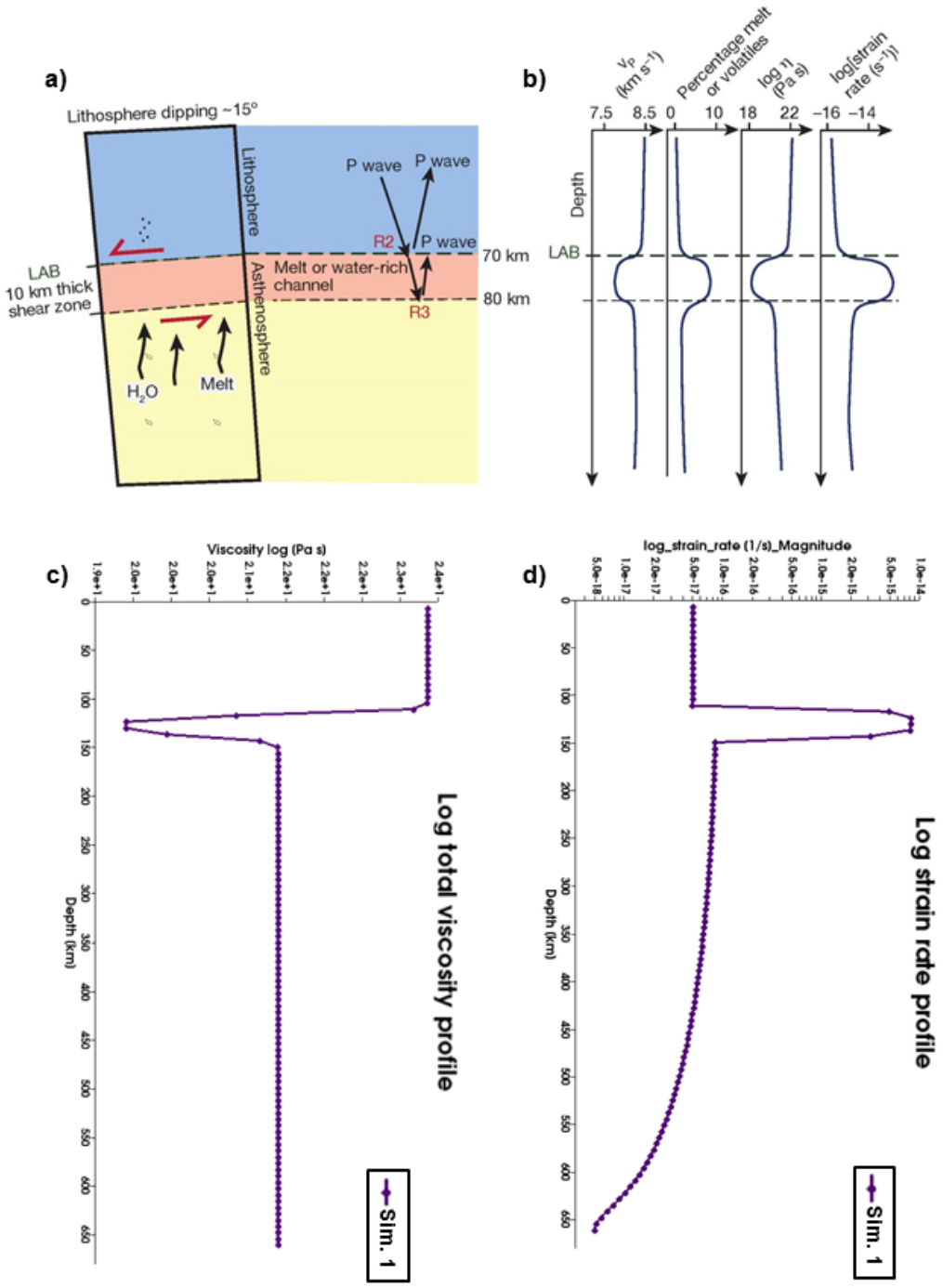

Fig. 35: a) and b) are schematic summaries showing the interpretation of physical properties at the base of the Pacific plate lithosphere from Stern et al. (2015). c) and d) illustrate the viscosity and strain rate plot obtained by the the analysis of Sim. 1 case.

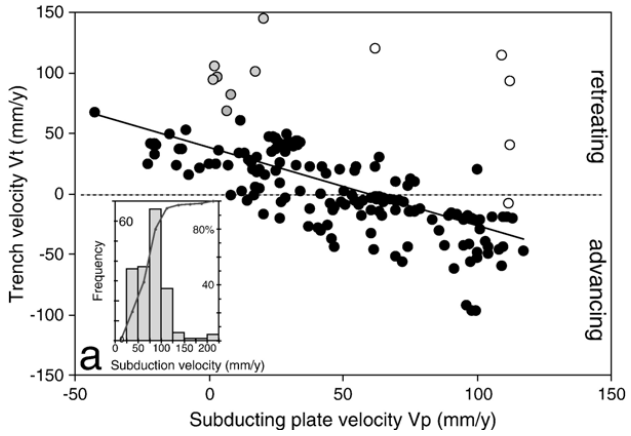

Fig. 36: Velocity field of the normal-to-trench component of subducting plate and trench velocity in the hot spot references frame (model HS3- NUVEL1A). The diagram illustrates that a fast retreating trench is generally associated to slow subducting plate motion (Faccenna et al. (2007)).

absolute frame of reference, for which no general agreement seems to exist. However, values ranging from 2 – 15 cm/yr are expected (see Schott and Schmeling (1998)). These potential lower than expected predicted values found in this study (from few millimetres to a few centimetres per second) are possibly due to the neglection of temperature as an influencing parameter. Further investigations which focus on viscosity and density variations arising from self-consistent treatment of the lithosphere as a visco-elasto-plastic body and growing boundary layer will be able to address how the morphologies of hinges evolve as they retreats back into progressively thinner or thicker oceanic lithosphere.

In accordance with Bellahsen et al. (2005), the Earth's dynamic system is in a delicate equilibrium for the interaction between the rigidity of the plate and the layering of the mantle. The plate tectonic mechanisms shows a large variety of configurations with episodes of collision and extension. This rather unique setting should be then responsible for the complex tectonic regimes observed on the Earth. The potential existence of high/low viscosity channels in the Earth's structure perhaps not only at the LAB could also provide the perturbation necessary to self- sustained our dynamic system.

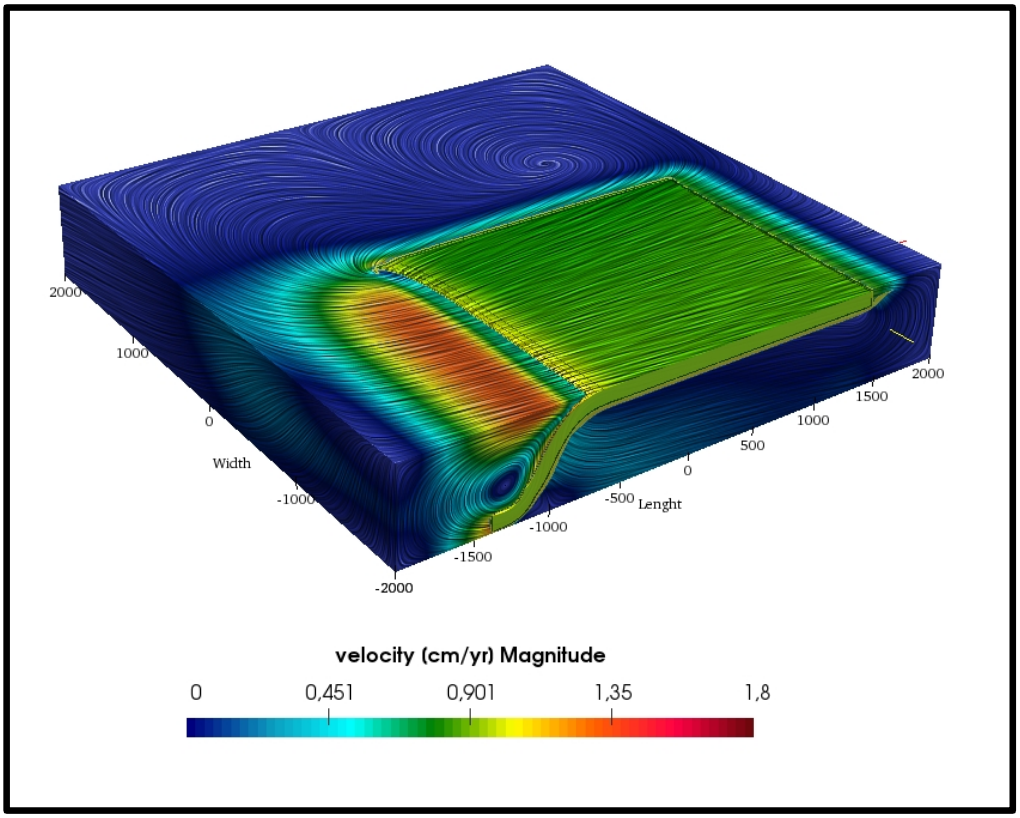

Fig. 37: Figure showing the development of the poloidal and toroidal components of the velocity field during subduction. Here, the effect of a weak layer is to increase the relative convergence velocity between the subducting plate and the mantle.

5 Conclusion

The question does a weak layer at lithosphere asthenosphere boundary play any role on subduction dynamics has been addressed by the 2-D and 3-D analysis and investigation of the first order effects. The investigation focussed on the effect of a WL in determining the shapes, mechanisms, velocities and the relative deformation flow of the process of an oceanic plate subducting into the mantle. The first order effects were developed as a consequence of the different parameters explored in this study, specifically the viscosity, density and thickness. As no previous geodynamics models on this topic exist, it was important to understand the first-order physical principles and effects. The coupled investigation of the mantle convection and plate tectonics mechanisms allowed to constrain the role of a weak layer on subduction dynamics within the scenario modelled in this thesis. The presence of a weak layer at the LAB can primarily generate a variety of subduction regimes. Four distinct types of subduction mechanisms were identified and classified based on the final stage of their long-term subduction evolution. Each of which has an associated trench and plate motion with resultant slab morphology, more specifically:

1. Type I: either 2-D or 3-D continuously retreating trench accompanied by predominantly slab roll back and a forward plate motion, resulting in a flat-lying slab (fig. 28 a).
2. Type II: a 2-D generally quasi stationary trench associated with a forward plate motion, resulting in a flat-lying slab (fig. 28 b).
3. Type III: a 2-D continuously advancing trench accompanied by predominant backwards plate motion that results in an overturned, flat-lying slab with a little recumbent fold (fig. 28 c).
4. Type IV: a 3-D generally quasi stationary trench associated by predominant backwards plate motion that results in an overturned, flat-lying slab with a little recumbent fold (fig. 28 d).

The type I subduction regime develops for the case of an oceanic plate subducting into the mantle with no weak layer. The type II develops for viscosity and density contrast values between mantle and weak layer which are intermediate between those for type I and type III subduction. Type III develops for a relatively high value of viscosity and density contrast between the mantle and the weak layer. Type IV develops in an equivalent 3-D case of the type II subduction.

Type VI subduction also revealed that the addition of a third dimension can play a role on the possible subduction mechanisms developed, demonstrating that both the toroidal and poloidal type circulations can significantly affect the evolution of the model.

The overall trend emerging from this study is that the presence of a weak layer at the LAB on subduction dynamics can promote an advancing trend for the plate, as seen in fig. 28 e).

Moreover, for the subduction regimes studied, it was possible to find a correlation between the total subducting velocity and the viscosity contrast, and also the density contrast between the mantle and the weak layer. The thickness however was observed to not to play a main role in defining the main subduction regimes. The total subduction velocity is linearly related to the viscosity contrast between mantle and the weak layer and inversely related to the density contrast between mantle and weak layer. It should be noted that other factors not considered here for simplicity could also play a role in defining the controls of the WL on the subduction dynamics.

Future investigations will concentrate on exploring the role of other factors, such as those involved for a temperature dependent visco-elasto-plastic rheology affecting the behaviour of the system. This would help to better address how the subduction regimes and velocities evolve through time as the oceanic plate moves into a progressively thinner (younger) or thicker (older) lithosphere. Also, the role of an overriding plate on the system will be another important factor to explore in the future, as the overall advancing nature of the models could be resisted by its additional physical presence.

The results modelled here are well suited to the localisation of the strain rate and the accommodation of the stress drop predicted at the LAB. This weak channel could represent a detachment layer that can accommodate the relative motion between an oceanic plate and underlying asthenospheric mantle.

In conclusion, the possible existence of a weak layer at the lithosphere asthenosphere boundary can affect the subduction dynamics, promoting an overall advancing trend for the oceanic plate and its trench, with both the resultant motions dependent on the constrained characteristics of the weak layer.

References

Xavier Le Pichon, Jean Francheteau, and Jean Bonnin. *Plate tectonics*, volume 6. Elsevier, 2013.

Patrick L Abbott. *Natural disasters*. McGraw-Hill New York, 2008.

Donald Forsyth and Seiya Uyeda. On the relative importance of the driving forces of plate motion. *Geophysical Journal International*, 43(1):163–200, 1975.

David Bercovici, Yanick Ricard, and Mark A Richards. The relation between mantle dynamics and plate tectonics: A primer. *The history and dynamics of global plate motions*, pages 5–46, 2000.

David Bercovici. The generation of plate tectonics from mantle convection. *Earth and Planetary Science Letters*, 205(3):107–121, 2003.

Yanick Ricard. Physics of mantle convection. *Treatise on geophysics*, 7: 31–87, 2007.

Donald L Turcotte and Gerald Schubert. *Geodynamics*. Cambridge University Press, 2014.

Nick Rogers and Stephen Blake. *An introduction to our dynamic planet*. Cambridge University Press, 2008.

Bradford H Hager and Richard J O'Connell. A simple global model of plate dynamics and mantle convection. *Journal of Geophysical Research: Solid Earth*, 86(B6):4843–4867, 1981.

Don L Anderson. Lithosphere, asthenosphere, and perisphere. *Reviews of Geophysics*, 33(1):125–149, 1995.

Irina M Artemieva and Walter D Mooney. On the relations between cratonic lithosphere thickness, plate motions, and basal drag. *Tectonophysics*, 358 (1):211–231, 2002.

Hitoshi Kawakatsu, Prakash Kumar, Yasuko Takei, Masanao Shinohara, Toshihiko Kanazawa, Eiichiro Araki, and Kiyoshi Suyehiro. Seismic evidence for sharp lithosphere-asthenosphere boundaries of oceanic plates. *Science*, 324(5926):499–502, 2009.

Karen M Fischer, Heather A Ford, David L Abt, and Catherine A Rychert. The lithosphere-asthenosphere boundary. *Annual Review of Earth and Planetary Sciences*, 38:551–575, 2010.

Nicholas Schmerr. The gutenberg discontinuity: Melt at the lithosphere-asthenosphere boundary. *Science*, 335(6075):1480–1483, 2012.

Tatsuya Sakamaki, Akio Suzuki, Eiji Ohtani, Hidenori Terasaki, Satoru Urakawa, Yoshinori Katayama, Ken-ichi Funakoshi, Yanbin Wang, John W Hernlund, and Maxim D Ballmer. Ponded melt at the boundary between the lithosphere and asthenosphere. *Nature Geoscience*, 6(12): 1041–1044, 2013.

Catherine A Rychert, Karen M Fischer, and Stéphane Rondenay. A sharp lithosphere–asthenosphere boundary imaged beneath eastern north america. *Nature*, 436(7050):542–545, 2005.

Catherine A Rychert, Peter M Shearer, and Karen M Fischer. Scattered wave imaging of the lithosphere–asthenosphere boundary. *Lithos*, 120(1): 173–185, 2010.

Catherine A Rychert and Peter M Shearer. Imaging the lithosphere-asthenosphere boundary beneath the pacific using ss waveform modeling. *Journal of Geophysical Research: Solid Earth (1978–2012)*, 116(B7), 2011.

Jerry X Mitrovica and Alessandro M Forte. Radial profile of mantle viscosity: results from the joint inversion of convection and postglacial rebound observables. *Journal of Geophysical Research: Solid Earth (1978–2012)*, 102(B2):2751–2769, 1997.

Catherine A Rychert. Earth science: The slippery base of a tectonic plate. *Nature*, 518(7537):39–40, 2015.

TA Stern, SA Henrys, D Okaya, JN Louie, MK Savage, S Lamb, H Sato, R Sutherland, and T Iwasaki. A seismic reflection image for the base of a tectonic plate. *Nature*, 518(7537):85–88, 2015.

Joaquim Peiró and Spencer Sherwin. Finite difference, finite element and finite volume methods for partial differential equations. In *Handbook of materials modeling*, pages 2415–2446. Springer, 2005.

Fabio Crameri and Boris JP Kaus. Parameters that control lithospheric-scale thermal localization on terrestrial planets. *Geophysical Research Letters*, 37(9), 2010.

Boris JP Kaus, Anton A Popov, Tobias S Baumann, Adina E Püsök, Arthur Bauville, Naiara Fernandez, and Marine Collignon. Forward and inverse modeling of lithospheric deformation on geological timescales. 2015.

Alik Ismail-Zadeh and Paul Tackley. *Computational methods for geodynamics*. Cambridge University Press, 2010.

Paul J Tackley. Modelling compressible mantle convection with large viscosity contrasts in a three-dimensional spherical shell using the yin-yang grid. *Physics of the Earth and Planetary Interiors*, 171(1):7–18, 2008.

Taras Gerya. *Introduction to numerical geodynamic modelling*. Cambridge University Press, 2009.

Aleksandr IAkovlevich Malkin, Alexander Ya Malkin, and Avraam I Isayev. ChemTec Publishing, 2006.

Boris Kaus. Advanced computational geodynamics class handout, 2014.

Gilbert Strang and George J Fix. *An analysis of the finite element method*, volume 212. Prentice-Hall Englewood Cliffs, NJ, 1973.

Olgierd Cecil Zienkiewicz and Robert Leroy Taylor. *The finite element method: solid mechanics*, volume 2. Butterworth-heinemann, 2000.

Francis H Harlow and J Eddie Welch. Numerical calculation of time-dependent viscous incompressible flow of fluid with free surface. *Physics of fluids*, 8(12):2182, 1965.

H Schmeling, AY Babeyko, A Enns, C Faccenna, F Funiciello, T Gerya, GJ Golabek, S Grigull, BJP Kaus, G Morra, et al. A benchmark comparison of spontaneous subduction models—towards a free surface. *Physics of the Earth and Planetary Interiors*, 171(1):198–223, 2008.

Alwina Enns, Thorsten W Becker, and Harro Schmeling. The dynamics of subduction and trench migration for viscosity stratification. *Geophysical Journal International*, 160(2):761–775, 2005.

DR Stegman, Justin Freeman, WP Schellart, L Moresi, and David May. Influence of trench width on subduction hinge retreat rates in 3-d models of slab rollback. *Geochemistry, Geophysics, Geosystems*, 7(3), 2006.

WP Schellart, Justin Freeman, DR Stegman, L Moresi, and David May. Evolution and diversity of subduction zones controlled by slab width. *Nature*, 446(7133):308–311, 2007.

F Funiciello, C Faccenna, A Heuret, Serge Lallemand, E Di Giuseppe, and TW Becker. Trench migration, net rotation and slab–mantle coupling. *Earth and Planetary Science Letters*, 271(1):233–240, 2008.

Nicolas Bellahsen, Claudio Faccenna, and Francesca Funiciello. Dynamics of subduction and plate motion in laboratory experiments: insights into the "plate tectonics" behavior of the earth. *Journal of Geophysical Research: Solid Earth*, 110(B1), 2005.

DR Stegman, Rebecca Farrington, FA Capitanio, and WP Schellart. A regime diagram for subduction styles from 3-d numerical models of free subduction. *Tectonophysics*, 483(1):29–45, 2010.

WP Schellart. Kinematics of subduction and subduction-induced flow in the upper mantle. *Journal of Geophysical Research: Solid Earth*, 109 (B7), 2004.

C Kincaid and RW Griffiths. Laboratory models of the thermal evolution of the mantle during rollback subduction. *Nature*, 425(6953):58–62, 2003.

Francesca Funiciello, Claudio Faccenna, Domenico Giardini, and Klaus Regenauer-Lieb. Dynamics of retreating slabs: 2. insights from three-dimensional laboratory experiments. *Journal of Geophysical Research: Solid Earth*, 108(B4), 2003.

Thorsten W Becker and Claudio Faccenna. A review of the role of subduction dynamics for regional and global plate motions. In *Subduction Zone Geodynamics*, pages 3–34. Springer, 2009.

Boris JP Kaus and Yuri Y Podladchikov. Initiation of localized shear zones in viscoelastoplastic rocks. *Journal of Geophysical Research: Solid Earth*, 111(B4), 2006.

Boris JP Kaus and Thorsten W Becker. Effects of elasticity on the rayleigh–taylor instability: implications for large-scale geodynamics. *Geophysical Journal International*, 168(2):843–862, 2007.

P Yamato, Laurent Husson, J Braun, C Loiselet, and C Thieulot. Influence of surrounding plates on 3d subduction dynamics. *Geophysical Research Letters*, 36(7), 2009.

Claudio Faccenna, Arnauld Heuret, Francesca Funiciello, Serge Lallemand, and Thorsten W Becker. Predicting trench and plate motion from the dynamics of a strong slab. *Earth and Planetary Science Letters*, 257(1): 29–36, 2007.

B Schott and H Schmeling. Delamination and detachment of a lithospheric root. *Tectonophysics*, 296(3):225–247, 1998.

Appendix A

The initial validation simulations were performed involving a 2D, simple geometrical and rheological models, using the MVEP2 code. The model setup developed for the MVEP2 models was taken from a literature benchmark paper of Schmeling et al. (2008) and is shown in fig. 38. The model has involved a linear viscous rheology and a free surface boundary condition at the top of the model whereas have free slip at all the others boundaries. The subducting plate is 100 km thick, 2000 km wide and 2750 km in length. The weak layer has the same dimension of the oceanic plate except for the thickness that is only 10 km. The WL is located below the oceanic plate and has a viscosity contrast in the respect to the mantle of 2 orders of magnitude.

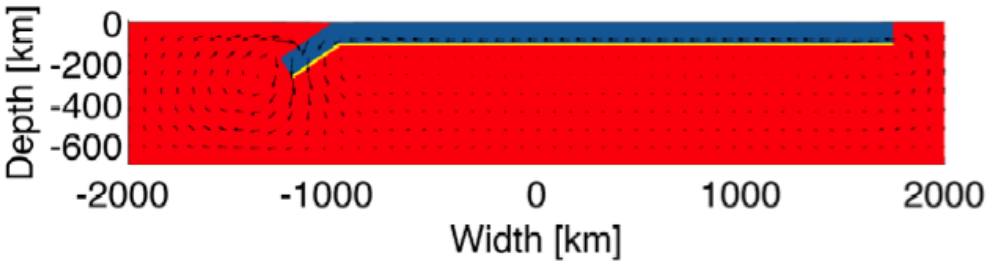

Fig. 38: Model setup used for the simulations performed with MVEP2 code. The thickness is only 10 km and has a viscosity contrast in the respect to the mantle of 2 orders of magnitude. The top box boundary has a free surface boundary condition and the other boundaries employ a free slip condition.

Fig. 39 and fig. 40 show the summarised important points from the results obtained using MVEP2, such as:

1. horizontal plate motion increases of a nearly factor two with a presence of a low viscous layer, fig. 39, a).

2. the slab tip motion increases slightly for the simulations involving a low viscous layer, fig. 39 b).

3. the trench tends to advance, fig. 39 c).

4. the slab tip depth motion and direction is affected by the decoupled effect of density and viscosity contrast between mantle and weak layer, fig. 40 a) and b) respectively.

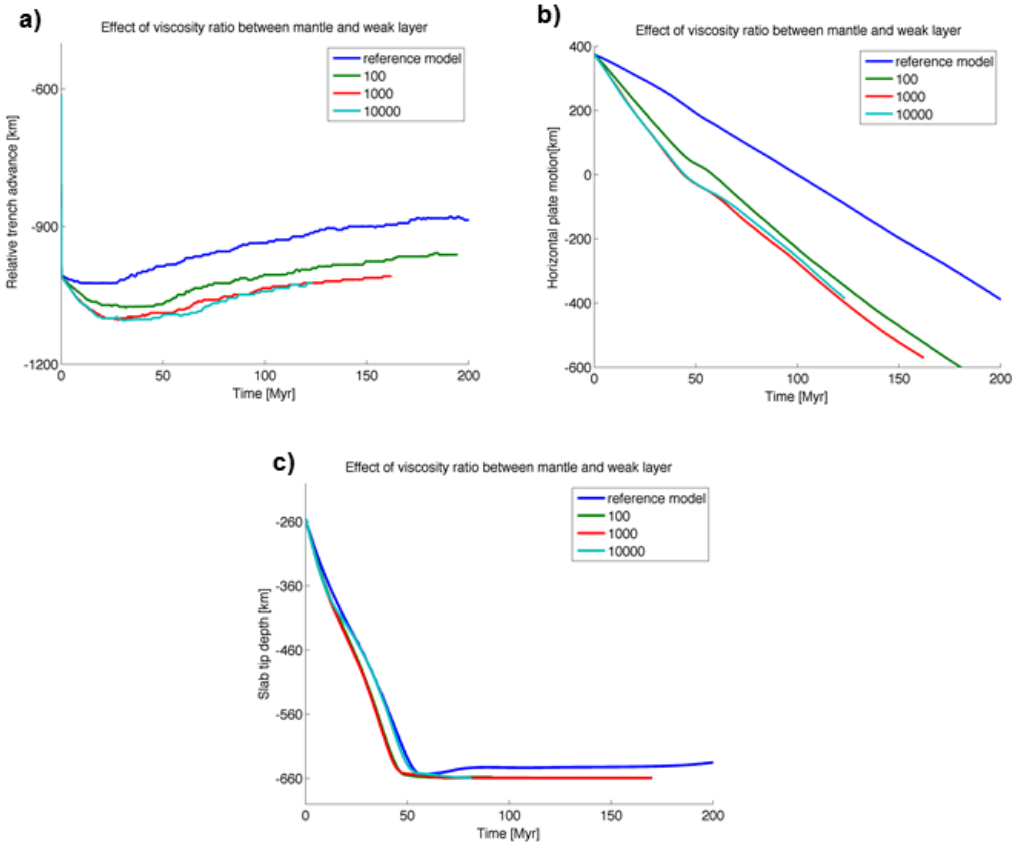

Fig. 39: graphs illustrating the effect of the viscosity contrast between mantle and weak layer on the trench motion, plate horizontal motion and slab tip depth in a), b) and c) respectively.

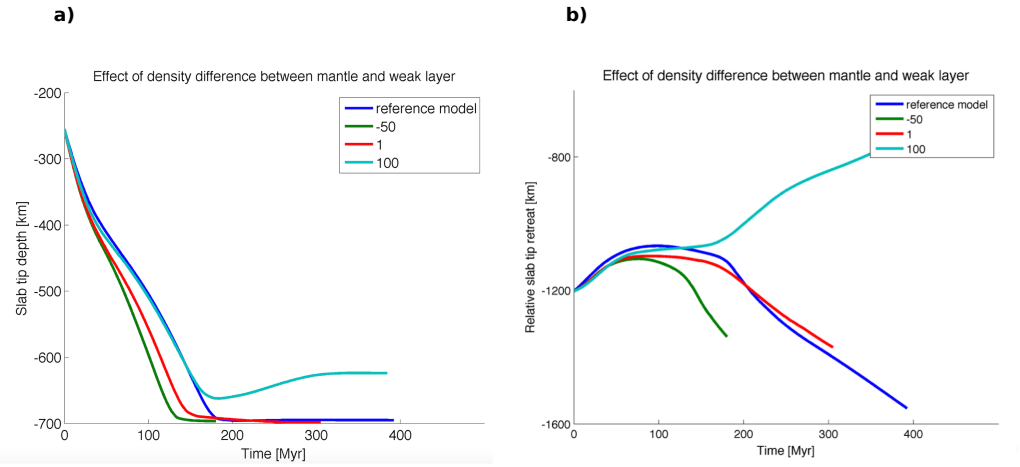

Fig. 40: Plots illustrating the effect of the density and viscosity contrast between mantle and weak layer on the slab tip depth vertical and horizontal motion in a) and b) respectively, for a constant $\eta_{mwl} = 2000$.

The simulations shown in fig. 41 b) d) and f) are the MVEP2 simulations correspondent of the simulation RM, Sim. 1 and Sim. 2 for the LaMEM code a) c) d) respectively in figure. Altough, In MVEP2 is modelled a fully linear viscous rheology case with a free surface boundary condition as a top of boundary condition and for the LaMEM case is modelled a visco-plastic problem involving free slip boundary conditions at all the boundaries of the model. The thickness of the weak layer is also only 10 km for the MVEP2 case and 30 km for the LaMEM simulations.

The comparison shown in fig. 41, reveal that a weak layer at the LAB can influence the motion of the plate and the trench. This is valid for both the codes. The main differences developed in the evolution of the models are:

1. the time needed for the slab tip to reach the bottom of the model (Δt $\approx$ 10-15 Myrs),

2. the different subduction regimes developed for the cases involving a viscosity contrast between the mantle and the weak layer of $\geqslant$ 103.

These differences are possible due to the fact that these are two different codes that employ two different numerical methods to solve the physical problem. However, the overall trend of the subduction dynamics involving a presence of a weak layer at the LAB is also respected for the MVEP2 models. A weak layer can influence the subduction dynamics, promoting the motion of the plate and the trench.
After the initially validation models developed using MVEP2, comparable 2-D results were obtained using LaMEM. During the development of the 3-D models, a numerical instability was encountered and is shown in fig. 42. This was not able to be overcome in the time available and so the model set-up was changed for the final analysis.

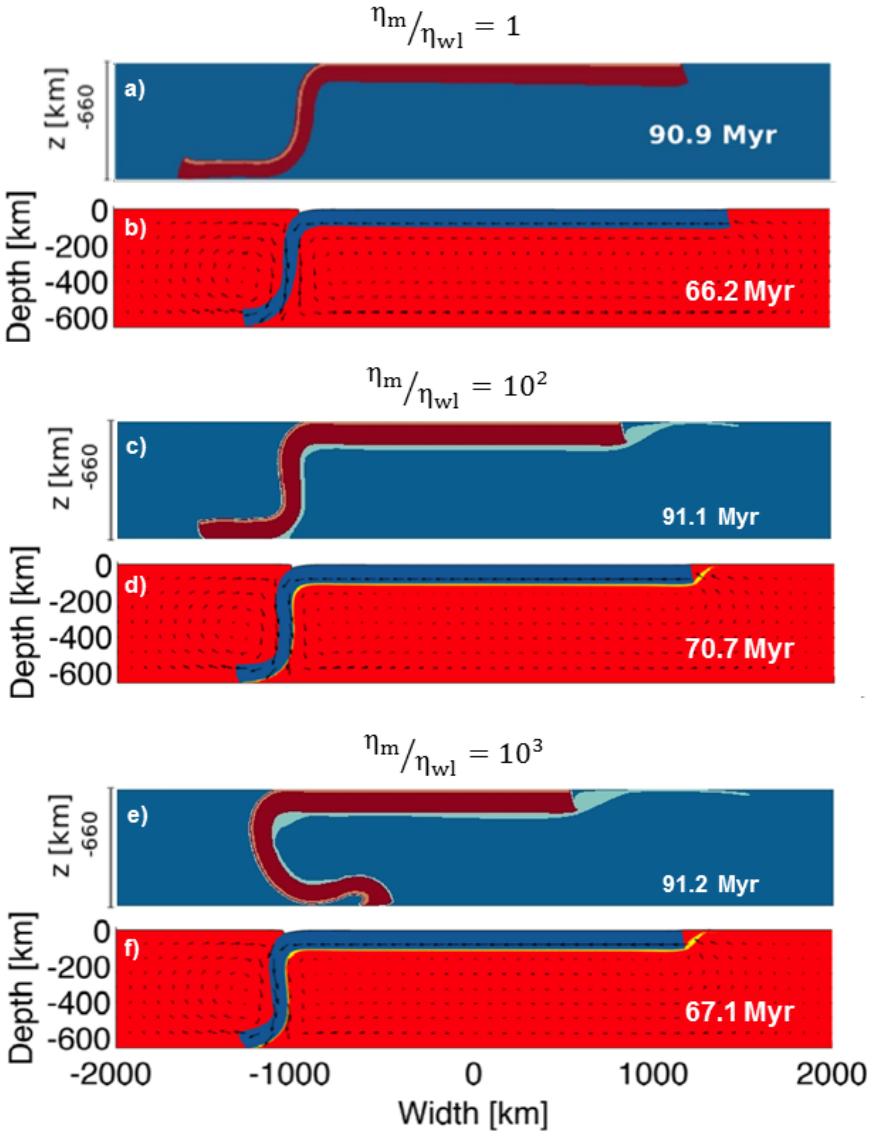

Fig. 41: Comparison showing the last stage of the phase field time evolution for the models having a $\eta_{mwl} = 10^0$, a) and b) for LaMEM and MVEP2 codes respectively; $\eta_{mwl} = 10^2$, c) and d) for LaMEM and MVEP2 codes respectively, $\eta_{mwl} = 10^3$, e) and f) for LaMEM and MVEP2 codes respectively.

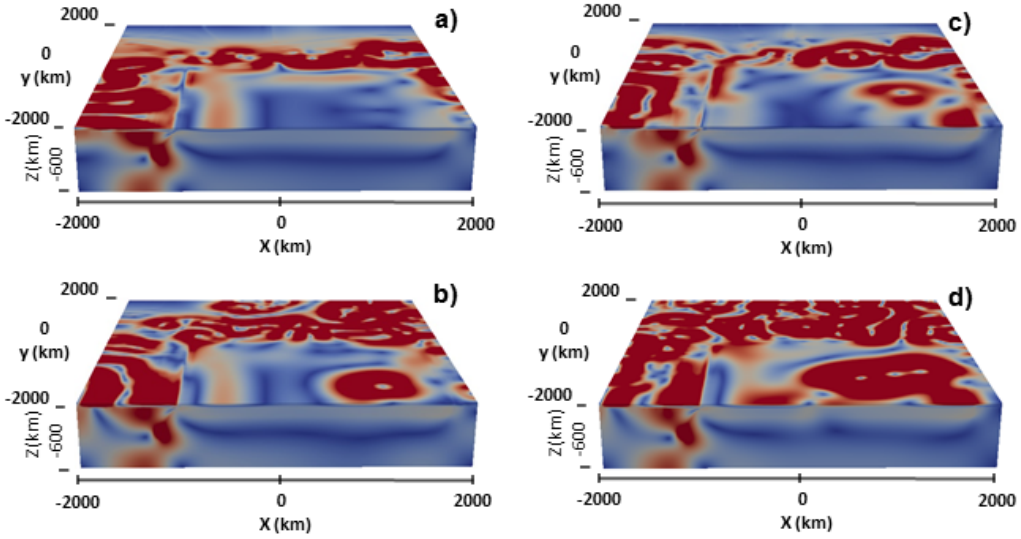

Fig. 42: Development of a free surface numerical instability in consecutive steps of the time evolution a), b), c) and d).

Acknowledgements

I would like to thank a number of key people who have been an integral part of this thesis. In particular, I would like to thank my thesis supervisors Prof. Boris Kaus and Dr. Manuele Faccenda, for their help and guidance. I am extremely grateful for the time, energy and patience they devoted to me – thanks to your support, you have allowed me to realise my own project.

My experiences during this internship have been instrumental in preparing me for whatever and wherever my life will take me. I believe this is the beginning of something that would have never have been possible without the support and training received. It was a pleasure to spend time with you both, and I hope to maintain a lasting friendship with many more opportunities for professional collaboration in the future.

I would also like to thank Anton Popov, Adina Püsök, Ragnar Lehmann and Jianfeng Yang, who were always happy to share their experience, and to provide help when needed. They have been a source of inspiration and guidance for me, and it has been an enormous pleasure to meet them. There was never a dull moment, and it was a fantastic experience to work in such a stimulating and exciting international environment.

I would personally like to thank both the University of Padova, and also the JGU University of Mainz, for facilitating the time I spent studying abroad and for providing me with the opportunity and facilities with which to undertake and complete my thesis.

Also, I would like to extend my thanks to all the friends I have made here in Mainz, who have given me so much support since I arrived nearly one and half year ago. In particular Josh Rose, Lisa Rummel and Ryan Garret. They were the ones who wiped away my tears, helped me to rebuild my shattered confidence during my lowest times and it was they who supported me each day. I would never have thought it was possible to meet such great people. So great, in fact, that I found it difficult to say farewell to Ryan in particular, and it will be difficult to leave all my friends in Germany behind.

Finally, I would like to say thank you to my family. Despite the difficulties we have encountered they have always been there to help me through my years' of study.

Thanks to support of everybody I've mentioned, and anybody I may have forgotten, I found the strength to maintain my self-believe and I never gave up. Everyone who knows me understands that I love challenging situations.